Doctor Dissertation

EELS Study on the Relationship between Oxygen Deficiency Sites and the Transition Temperature of YBCO

Liu Xiaopeng

Supervisor: Oshima Yoshifumi

Graduate School of Advanced Science and Technology

Japan Advanced Institute of Science and Technology

Materials Science

September 2025

Abstract

The superconducting transition temperature (T_c) in $YBa_2Cu_3O_{7-\delta}$ (YBCO) is known to exhibit a strongly nonlinear dependence on the oxygen deficiency parameter δ. While this behavior has long been associated with the distribution of oxygen vacancies among different crystallographic sites—particularly the Cu–O chains and CuO_2 planes—the lack of direct, spatially resolved experimental data has limited our understanding of the underlying mechanisms. In this study, we employed scanning transmission electron microscopy combined with electron energy-loss spectroscopy (STEM-EELS) to investigate the site-specific oxygen deficiencies in a series of YBCO thin films with different T_c values (49 K, 64 K, 81 K, and 86 K). Our goal was to elucidate how the spatial distribution of oxygen deficiencies affects superconducting properties, and in particular, to understand the origin of the well-known 60 K plateau in the T_c–δ phase diagram.

The YBCO thin films were synthesized by pulsed laser deposition (PLD) on $LaAlO_3$ (001) substrates and subjected to post-deposition annealing under various oxygen pressures to systematically control the oxygen content. Cross-sectional STEM specimens were prepared using focused ion beam (FIB) milling and low-energy Ar^+ ion polishing to ensure high-quality, damage-free lamellae. High-angle annular dark field (HAADF) imaging was used to identify structural features and guide site-specific EELS measurements. EELS spectra were acquired at atomic resolution, and changes in the pre-peak of the O K-edge—associated with hybridized O 2p–Cu 3d states—were used as a sensitive indicator of local oxygen deficiency.

Our results reveal that in YBCO thin films with $T_c \approx 81$ K and 64 K, oxygen deficiencies predominantly occur at the Cu–O chain sites, while the CuO_2 planes remain relatively intact. In contrast, in the more heavily deoxygenated sample with $T_c \approx 49$ K, significant oxygen loss is observed at both the Cu–O chains and the CuO_2 planes. This transition from chain-only to chain-plus-plane deficiency correlates with a sharp suppression of T_c, consistent with theoretical models suggesting that the electronic structure of the CuO_2 planes is directly responsible for superconductivity, while the Cu–O chains primarily act as a charge reservoir.

These findings provide direct experimental evidence linking the spatial distribution of oxygen deficiencies to the superconducting properties of YBCO. Furthermore, they offer a plausible explanation for the persistence of the 60 K plateau: as long as oxygen loss is confined to the Cu–O chains, the hole concentration in the CuO_2 planes remains relatively stable, preserving superconductivity around 60 K despite variations in δ. Only when oxygen deficiencies begin to affect the CuO_2 planes directly does T_c drop significantly. This work highlights the unique capability of STEM-EELS to resolve local structure–property relationships at the atomic scale and provides new insights into the microscopic origins of superconductivity modulation in high-T_c cuprates.

Key words: YBCO, transition temperature,60 K,STEM-EELS, oxygen deficiency.

.

Content

Abstract.....

Chapter 1. Introduction..... 1

1.1 Overview of YBCO superconductors..... 1

1.1.1 The Origins of Superconductivity 1

1.1.2 High-Temperature Superconductors..... 7

1.1.3 Structure of YBCO 9

1.1.4 Valence States and Cu–O Hybridization in YBCO 11

1.2 Influence of oxygen content on T_c of YBCO..... 13

1.3 Previous study on T_c of YBCO..... 16

1.4 Advanced Characterization of Oxygen Deficiency in Oxides..... 18

1.5 Research Objectives 25

Chapter 2.Theoretical Framework..... 27

2.1 Basics of Scanning Transmission Electron Microscopy (STEM) 27

2.1.1 Fundamentals and Instrumentation of STEM..... 27

2.1.2 Electron–Specimen Interaction in STEM..... 29

2.1.3 Ronchigram and Its Role in Aberration Correction..... 31

2.1.4 High-Angle Annular Dark Field (HAADF) Imaging 34

2.2 Basics of Electron Energy Loss Spectroscopy (EELS) 36

2.2.1 Fundamentals of EELS and Energy-Loss Mechanisms 36

2.2.2 Core-Loss Region and Fine Structures 40

2.2.3 Advantages and Spatial Resolution in STEM-EELS 43

Chapter 3 Experimental Methods 46

3.1 Fabrication and Oxygen Control of YBCO Thin Films 46

3.1.1 Rationale for Using Thin Films Instead of Bulk Single Crystals 48

3.2 Preparation of Cross-Sectional STEM Specimens 50

3.3 Experimental Setup for STEM-EELS Analysis 52

3.4 Methodology for Mapping Oxygen Deficiencies 54

3.4.1 Spectrum Image Acquisition 54

3.4.2 Preprocessing and Denoising 55

3.4.3 Pre-Peak Integration for δ Mapping 55

3.4.4 Spatial Correlation with Structural Features 56

3.4.5 Quantification Strategy and Limitations 57

Chapter 4 Atomic-Scale Characterization of Oxygen Deficiency in YBCO Thin Films 64

4.1 Structural Characterization by XRD and STEM Imaging 64

4.1.1 X-ray Diffraction (XRD) Analysis 64

4.1.2 STEM-HAADF Imaging 67

4.2 Electronic structure analysis by EELS: O K-edge and Cu L-edge 69

4.3. Site-specific oxygen deficiency and T_c 73

4.4 Representativeness of the EELS Analysis Region 77

4.5 Reproducibility of Site-Specific EELS Spectra at $T_c \approx 49$ K 80

Chapter 5. Conclusion and Outlook 83

5.1 Summary of Key Findings 83

5.2 Research Contributions 84

5.3 Outlook and Future Directions 85

Reference 87

Acknowledgement 96

Achievements 97

Chapter 1. Introduction

1.1 Overview of YBCO superconductors

1.1.1 The Origins of Superconductivity

Kamerlingh Onnes discovered superconductivity (1911) and the observation of zero resistance in mercury at 4.2 K. Superconductivity was first identified when Kamerlingh Onnes investigated the electrical properties of mercury at extremely low temperatures. This discovery was made possible by his earlier achievement in successfully liquefying helium in 1908, which allowed him to conduct experiments at temperatures close to absolute zero. In his laboratory, Onnes observed that when mercury was cooled below a certain threshold temperature (around 4.2 K),[1] as the Fig 1.1 shown, its electrical resistance abruptly disappeared, a phenomenon that he coined “supraconductivity.” Prior to Onnes’s work, there were prevailing theories about the behavior of metals at low temperatures, most notably by Lord Kelvin, who suggested that the resistance of a metal would either approach zero or increase indefinitely as the temperature decreased. Onnes’s experiment with mercury disproved these theories, as he found that resistance in certain metals did not simply reduce to a minimum value but instead completely vanished. This result was unexpected and marked a fundamental shift

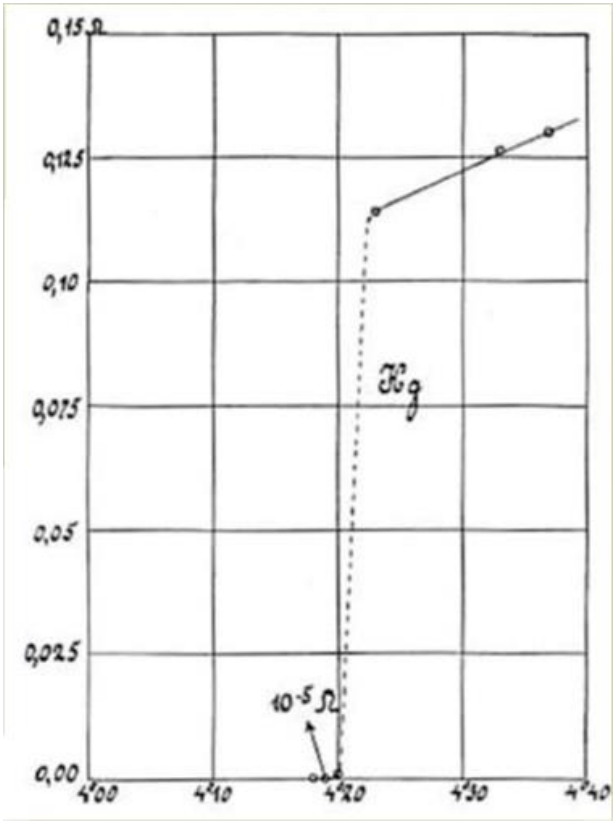

Fig.1.1 The original resistance–temperature curve of mercury (Hg) measured by Heike Kamerlingh Onnes in 1911. As the temperature decreases toward 4.2 K, the resistance of mercury drops abruptly to nearly zero ($10^{-5}\,\Omega$ or less), marking the discovery of superconductivity. This historical graph provides the first experimental evidence for the superconducting state.[1]

in the understanding of electrical conductivity. The implications of Onnes's discovery were profound, laying the groundwork for a new branch of physics. The phenomenon of superconductivity was observed in other materials, such as lead and tin, confirming the

reproducibility of the effect. Although the practical applications of superconductivity were initially limited by the need for very low temperatures (requiring liquid helium for cooling), the discovery sparked further research into the mechanisms behind superconductivity and its potential uses. Kamerlingh Onnes's work earned him the Nobel Prize in Physics in 1913, and his findings have since become a cornerstone of condensed matter physics, influencing countless studies and technological innovations in the field.[2]

Following the discovery of superconductivity, one of the key challenges was to develop a theoretical framework that could accurately describe its electromagnetic properties. While the phenomenon of zero electrical resistance was remarkable, an equally intriguing observation emerged with the discovery of the Meissner effect in 1933.[3] This effect demonstrated that superconductors expel magnetic fields from their interiors in the Fig.1.2, a behavior that could not be explained solely by perfect conductivity.

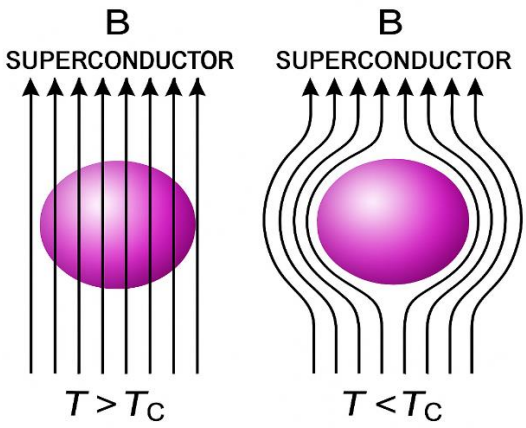

Fig 1.2 The figure of the superconductor with the magnetic field, when the T>

T_c, the magnetic flux lines can go through the superconductor, and when the $T<T_c$, the magnetic flux is expelled by the superconductor.

To address this gap, Fritz and Heinz London proposed the London equation in 1935, marking a pivotal advancement in the understanding of superconductivity. [4] The London equation mathematically describes how the supercurrent density is related to the magnetic field and vector potential within a superconductor.

$$\frac{\partial J}{\partial t} = \frac{nse^2}{m} E$$

where J is the current density; E is the electric field; ns is the density of superconducting

This equation describes the time evolution of the current density J in response to an applied electric field E within a superconductor. In contrast to normal conductors, where electrons experience scattering and resistance, the charge carriers in a superconductor (Cooper pairs) accelerate continuously under an electric field without any loss, indicating zero resistivity.

$$\nabla \times J = -\frac{n_s e^2}{m} B$$

where B is the magnetic field.

The second equation relates the curl of the current density to the magnetic field B. It implies that any magnetic field present in a superconductor decays exponentially from the surface into the interior, resulting in the exclusion of magnetic flux from the bulk of the material. This is a direct theoretical representation of the Meissner effect.

They provided the first quantitative explanation for the Meissner effect by showing that magnetic fields decay exponentially inside superconducting materials, with the penetration depth emerging as a critical parameter.[5] This insight not only explained why superconductors exhibit perfect diamagnetism but also highlighted the interplay between quantum mechanics and electrodynamics in governing superconducting behavior. By extending the classical framework to incorporate quantum mechanical principles, the London equation bridged the gap between experimental observations and theoretical understanding. They laid the foundation for subsequent advances in superconductivity, including the development of microscopic theories such as BCS theory. The London equation remains a cornerstone of superconductivity research, encapsulating the macroscopic properties of this quantum phenomenon in a simple yet powerful

mathematical form.[6,7]

Building on the phenomenological advancements like the London equation, the microscopic foundation of superconductivity was established in 1957 through the BCS theory, named after John Bardeen, Leon Cooper, and Robert Schrieffer. The BCS theory provided a revolutionary explanation for the superconducting state, describing it as a macroscopic quantum phenomenon arising from electron pairing. [8,9] At the core of the BCS theory lies the concept of Cooper pairs, where two electrons with opposite spins and momenta form a bound state mediated by phonon interactions. This pairing occurs despite the natural repulsion between electrons, as the attractive force introduced by lattice vibrations (phonons) dominates under certain conditions. These pairs of electrons condense into a collective quantum state, minimizing the system's energy compared to the normal metallic state.[10,11]

The formation of Cooper pairs explains key features of superconductivity. For instance, the energy gap required to break these pairs ensures the absence of resistive losses, while also resulting in the exponential suppression of electronic specific heat at low temperatures.[12,13] The BCS theory further elucidated the Meissner effect by linking it to the coherent behavior of paired electrons, which expel magnetic fields from the interior of a superconductor.[14] Additionally, the theory predicted the universal ratio of the energy

gap to the critical temperature,$2\Delta(0)/k_BT_c \approx 3.5$, which has been confirmed experimentally for conventional superconductors.[15]

The BCS framework also addressed the isotope effect, demonstrating that the critical temperature T_c depends inversely on the square root of the isotopic mass, further supporting the role of electron-phonon coupling.[16,17] This success in reconciling experimental observations with theoretical predictions marked the BCS theory as a cornerstone of condensed matter physics. Its principles not only explained conventional superconductivity but also paved the way for exploring unconventional superconductors, including high-temperature systems like YBCO.[18]

By connecting microscopic interactions to macroscopic phenomena, the BCS theory completed the foundational understanding of superconductivity that began with the London equation. It remains a seminal work, influencing both theoretical and experimental advances in the field.

1.1.2 High-Temperature Superconductors

The term high-temperature superconductors (HTS) refers to materials that exhibit superconductivity at temperatures significantly higher than those of conventional superconductors, which typically require cooling to below 20 K using liquid helium. In

contrast, HTS materials can maintain their superconducting state above the boiling point of liquid nitrogen (77 K),[19,20] making them far more practical and cost-effective for large-scale applications.

The discovery of high-temperature superconductivity in 1986 by Bednorz and Müller in the La–Ba–Cu–O system marked a turning point in condensed matter physics. Their work revealed that superconductivity could be achieved at 35 K in copper-oxide-based compounds (cuprates), breaking the long-standing upper limit of critical temperature predicted by the BCS theory. Just one year later, $YBa_2Cu_3O_{7-\delta}$ (YBCO) was found to exhibit superconductivity above 90 K, placing it firmly within the liquid nitrogen regime. This breakthrough ignited a surge of research into unconventional superconductors and earned Bednorz and Müller the Nobel Prize in Physics in 1987.[21,22]

From an application perspective, the elevated critical temperature of HTS materials has profound implications. Devices such as superconducting cables, fault current limiters, magnetic levitation systems, and high-field magnets benefit from reduced cooling costs and increased feasibility when liquid nitrogen is used instead of helium. Additionally, HTS materials are of particular interest in the development of quantum computers, energy storage systems, and next-generation particle accelerators.[23,24]

Despite these advantages, challenges remain, including the difficulty of fabricating

large, defect-free single crystals and ensuring long-term stability in real-world environments. Understanding the intrinsic properties of HTS, especially the effects of lattice structure, chemical composition, and defects such as oxygen vacancies, is crucial for optimizing their performance and enabling broader adoption.

1.1.3 Structure of YBCO

$YBa_2Cu_3O_{7-\delta}$ (YBCO) belongs to the family of copper-oxide-based high-temperature superconductors, known for their layered perovskite-like crystal structures.[25,26] The unit cell of YBCO is orthorhombic and consists of alternating layers stacked along the c-axis, as shown in Fig.1.3

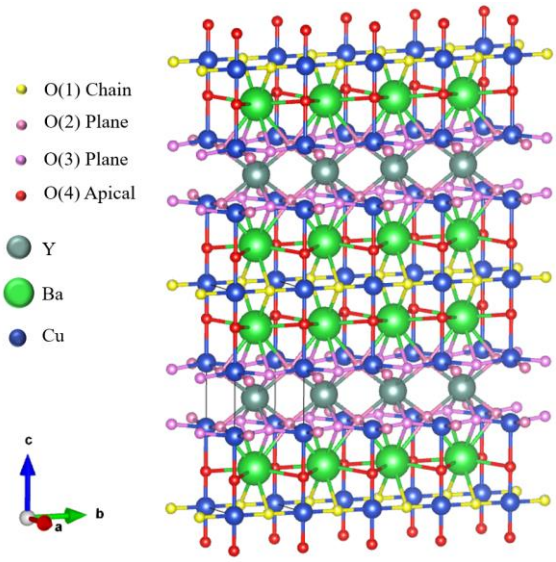

Fig.1.3 Crystal structure of $YBa_2Cu_3O_{7-\delta}$ (YBCO) viewed along the a-axis.

The structure can be described as a sequence of the following atomic planes:

- CuO_2 planes (in red and blue) that are crucial for superconductivity,
- Yttrium (Y) layers (gray spheres) sandwiched between CuO_2 planes,
- Cu–O chains (red/yellow horizontal rows) are responsible for charge reservoir behavior,
- BaO layers (green and pink framework) separating the CuO_2 planes and Cu–O chains.
- The Cu atoms exist in two distinct coordination environments:
- Cu(1) sites in the Cu–O chains (planar coordination),
- Cu(2) sites in the CuO_2 planes (square planar coordination).

Oxygen atoms (red spheres) in the Cu–O chains are particularly sensitive to oxygen deficiency (δ), and their removal can cause significant changes in the lattice symmetry (orthorhombic to tetragonal), carrier concentration, and ultimately the superconducting properties.

Notably, the CuO_2 planes are widely recognized as the active layers where Cooper pairing occurs, while the Cu–O chains serve as a charge reservoir that injects holes into the planes. The degree of oxygen ordering and deficiency in the chains strongly influences the hole doping level in the CuO_2 planes, and thereby determines the superconducting

transition temperature (T_c). This unique coupling between structural and electronic degrees of freedom makes YBCO an important model system for understanding high-T_c superconductivity.

1.1.4 Valence States and Cu–O Hybridization in YBCO

The electronic configuration of $YBa_2Cu_3O_{7-\delta}$ (YBCO) is governed by the oxidation states of its constituent elements and the hybridization between copper and oxygen orbitals. These factors define the bonding nature and electron distribution within the crystal structure.

In the fully oxygenated composition ($\delta \approx 0$), the typical formal oxidation states of the elements in YBCO are as follows: Yttrium (Y^{3+}): Occupies the central layer between the CuO_2 planes; chemically stable and does not participate in conduction. Barium (Ba^{2+}): Located adjacent to the Cu–O chains; contributes structurally. Oxygen (O^{2-}): Forms the lattice framework and completes the coordination environment of Cu. Copper (Cu): Exists in two distinct crystallographic sites: Cu(1): Located in the Cu–O chains. Cu(2): Located in the CuO_2 planes.[27,28]

For overall charge neutrality, the average oxidation state of copper in $YBa_2Cu_3O_7$ is

approximately +2.33, indicating a mixed-valence configuration involving both Cu^{2+} and Cu^{3+}. This fractional valence reflects a delocalized electronic structure, rather than discrete oxidation states at individual Cu sites.

The specific valence of Cu atoms depends on their coordination environment and oxygen occupancy. Cu tends to fluctuate between Cu^{+} and Cu^{2+} depending on oxygen content in the chains, while Cu typically lies between Cu^{2+} and Cu^{3+} in the planes.

The hybridization between Cu 3d orbitals and O 2p orbitals is a defining feature of the electronic structure in YBCO. This hybridization occurs both in the CuO_2 planes and in the Cu–O chains, but with distinct geometrical and orbital characteristics. In the CuO_2 planes, each Cu atom is coordinated by four in-plane oxygen atoms, forming a square-planar geometry. The dominant orbital interaction involves: Cu 3d orbitals, and O 2p orbitals, aligned along the Cu–O bond axes. This geometry facilitates strong σ-type (sigma-type) covalent hybridization, resulting in extended electronic states across the ab-plane. The bonding interaction defines the planar electronic structure and contributes to the delocalization of electronic states within the lattice. In the Cu–O chains along the b-axis, Cu atoms are linearly coordinated with O atoms. The relevant hybridization involves: Cu 3d orbitals and O 2p orbitals along the chain direction.[29]

The hybridization in the chains is generally weaker and more anisotropic than in the

CuO_2 planes, due to the quasi-one-dimensional configuration. Nevertheless, covalent bonding is still present and contributes to the overall charge distribution within the structure.

1.2 Influence of oxygen content on T_c of YBCO

The superconducting transition temperature (T_c) is one of the most important physical parameters used to evaluate the properties of superconducting materials. It defines the temperature below which the material exhibits zero electrical resistance and perfect diamagnetism, and thus marks the boundary between normal and superconducting states. In both basic research and practical applications, achieving a higher T_c is always desirable, as it allows superconductivity to occur under less extreme cooling conditions.

For real-world technologies, such as power transmission cables, magnetic levitation systems, and superconducting magnets, superconductors that operate above the boiling point of liquid nitrogen (77 K) are especially attractive, since they can significantly reduce cooling costs. Therefore, increasing T_c, or understanding how it can be tuned and stabilized, is critical to the widespread use of superconducting materials.

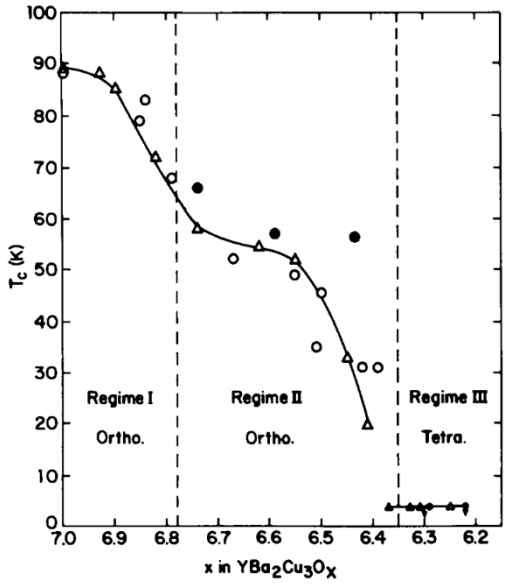

Fig.1.4 The relationship between oxygen deficiency distribution and T_c in $YBa_2Cu_3O_x$ thin films, correlated with oxygen concentration (x, which means 7-δ in this paper). [30]

The T_c of $YBa_2Cu_3O_{7-\delta}$ (YBCO) is strongly dependent on the oxygen deficiency parameter δ, which ranges from 0 (fully oxygenated) to ~1 (oxygen-deficient limit). Changes in δ alter the copper oxidation states and the concentration of mobile holes in the CuO_2 planes, thereby modulating the superconducting properties of the material. Notably, T_c exhibits a nonlinear response to variations in δ, as shown in the characteristic T_c–δ phase diagram in Fig.1.4.

In the fully oxygenated state ($\delta \approx 0$), the crystal structure is orthorhombic with well-

ordered Cu–O chains. This configuration supports optimal charge transfer from the Cu–O chains to the CuO_2 planes, leading to a maximum T_c of ~92 K, corresponding to the optimally doped regime. This is the most stable superconducting state of YBCO under ambient pressure.

As δ increases modestly (e.g., $\delta \approx 0.07$ to 0.3), the material enters the slightly underdoped regime. Surprisingly, instead of a continuous decline, T_c remains nearly constant around 60 K, forming a well-known plateau in the phase diagram. This behavior suggests that partial oxygen ordering in the Cu–O chains can sustain a relatively stable hole concentration in the CuO_2 planes over a wide δ range. The presence of this 60 K plateau is a distinctive and reproducible feature of the YBCO system. Beyond $\delta \approx 0.3$, YBCO enters the heavily underdoped regime. Here, the Cu–O chains become increasingly disordered or fragmented, and the orthorhombic structure begins to distort toward tetragonal symmetry. The hole concentration in the CuO_2 planes decreases rapidly, resulting in a nonlinear suppression of T_c, which drops below 30 K as δ approaches ~0.6. Superconductivity is eventually entirely suppressed near $\delta \approx 0.65$, marking the boundary with the non-superconducting or insulating phase.[31–33]

This overall T_c–δ relationship is strongly nonlinear and cannot be adequately captured by simple linear models. Theoretical calculations, such as those by Tallon et al.,

successfully reproduce both the 60 K plateau and the steep T_c drop in the underdoped regime. These features emphasize the intricate role of oxygen ordering, copper valence states, and interlayer charge redistribution in determining the superconducting behavior of YBCO.

1.3 Previous study on T_c of YBCO

Early research, such as that by Farneth et al. (1988) revealed three distinct regimes in the T_c vs. δ curve in Fig.1.4: a high-T_c orthorhombic regime, a 60 K plateau associated with partially ordered oxygen chains, and a non-superconducting tetragonal phase at low oxygen content.[30] This work emphasized that T_c is not only a function of total oxygen content but also depends strongly on oxygen ordering, especially within the Cu–O chains.

Later studies, such as Raven et al. (1994), explored strain effects in YBCO thin films and observed that T_c can decrease significantly without large changes in lattice constants.[34] This observation hinted at the importance of electronic structure, particularly hole concentration in the CuO_2 planes, over geometric distortion alone. A major breakthrough came from Liang, Bonn, and Hardy (2006), who proposed using the c-axis lattice parameter as a proxy for hole concentration rather than δ.[35] They reconstructed a more accurate T_c–p (hole doping level) phase diagram, explaining the well-known 60 K

plateau as an intrinsic electronic feature not fully captured by δ-based models.

In parallel, Zaleski and Kopeć (2006) offered a theoretical interpretation of the 60 K plateau, attributing it to interlayer charge imbalance and phase decoherence between underdoped planes and overdoped chains.[36] Their multicomponent XY phase model accounted for the emergence of distinct superconducting channels in different structural units of YBCO, further emphasizing the role of site-specific electronic interactions.

Despite these advances, several important questions remain unanswered:

- How are oxygen deficiencies spatially distributed among the different atomic sites?
- What is the microscopic mechanism by which chain-site disorder alters hole doping in the planes?
- Can we directly correlate local oxygen deficiency with local variations in T_c?
- How does oxygen behave at thin-film interfaces or strained heterostructures?
- Are structural transitions and electronic inhomogeneities coupled at the nanoscale?

To answer these, it is necessary to go beyond bulk measurements and average δ values, using techniques capable of revealing spatially resolved, site-specific information.

The T_c of $YBa_2Cu_3O_{7-\delta}$ (YBCO) exhibits a complex, highly nonlinear dependence on its oxygen deficiency δ. Extensive experimental and theoretical work has investigated how oxygen stoichiometry modulates lattice symmetry, copper valence states, and hole

concentration in the CuO_2 planes, thereby controlling the emergence, suppression, and optimization of superconductivity. Of particular interest is the presence of a characteristic plateau around 60 K in the T_c and δ phase diagram, which remains a key topic in cuprate research. This section reviews several landmark studies that have shaped our understanding of these phenomena, with attention to their methodologies, results, and limitations.

1.4 Advanced Characterization of Oxygen Deficiency in Oxides

For the characterization of oxygen deficiency in YBCO, there are two aspects that can be considered: one is from the crystal structure, and the other is from the electronic structure.

From the perspective of crystal structure analysis, transmission electron microscopy (TEM) is a powerful technique for characterizing local structural features in YBCO. Several studies have utilized TEM to visualize microstructural elements such as twin boundaries, dislocations, and phase distributions in YBCO (He et al., 1992)[37], and to examine the distribution of Y-211 particles using large-area TEM methods (Suematsu et al., 1998)[38]. However, directly locating individual oxygen vacancies in YBCO using TEM remains challenging. This difficulty arises because oxygen atoms are light and scatter electrons weakly, making them hard to detect directly in conventional TEM imaging. In

some studies, such as those by Basu et al., electron irradiation in TEM was used to induce and monitor oxygen disordering via diffraction pattern changes, rather than directly visualizing individual vacancies (Basu et al., 1989).[39] Thus, while TEM offers insights into structural consequences of oxygen deficiencies, direct site-specific observation of oxygen atoms or vacancies remains technologically limited.

X-ray diffraction (XRD) is a valuable tool for assessing the crystallinity of YBCO. Several previous studies have demonstrated that XRD can serve as an indirect method to estimate oxygen content by detecting subtle changes in lattice parameters. For instance, Degoy et al. found a linear relationship between XRD intensity ratios (I_{006}/I_{005}) and deviations in Ba and Cu stoichiometry, which correlate with oxygen content variations (Degoy et al., 1996).[40] Similarly, Benzi et al. demonstrated that oxygen content could be inferred from the c-axis parameter using XRD data, matching results obtained by iodometric titration (Benzi et al., 2004).[41] Additionally, Yurtcan et al. showed how varying oxygen pressure during film deposition affected the XRD patterns and indirectly the oxygen stoichiometry and phase purity of YBCO thin films (Yurtcan et al., 2013).[42]

However, a notable limitation of XRD is that it provides only average structural information across the sample. As a result, it is not capable of revealing site-specific variations in oxygen distribution.

To investigate the oxygen deficiency site, Jorgensen et al. (1990) employed neutron powder diffraction to systematically investigate oxygen site occupancies.[43]

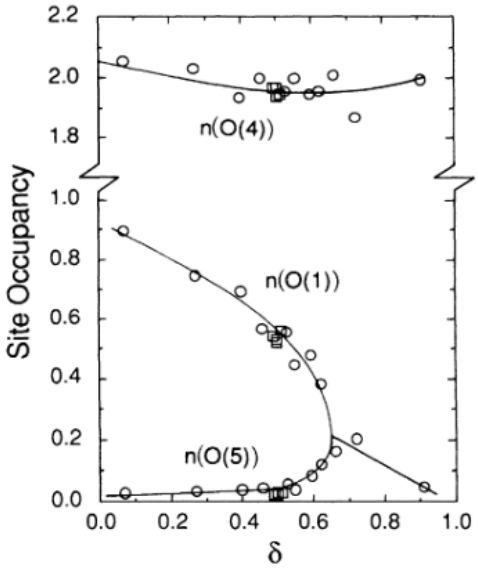

Fig.1.5. Oxygen site occupancies for the O(1), O(4), and O(5) sites in YBa_2Cu_3O7, here O(1) means the oxygen in the chain site, O(4) means the oxygen in the apical site, and O (5) means the oxygen in the simulation case.[43]

In the Fig.1.5, we can find the O (1) which represents the chain site has been changed a lot, while the O (4) which represents the apical site has been stable. Their analysis showed that oxygen deficiencies form preferentially at the Cu–O chain sites, while the apical sites remain almost fully occupied across all δ values. Importantly, their work suggested that apical oxygen has minimal influence on T_c, challenging earlier assumptions. Relying on

their work, people could focus our research particularly on the Cu-O chain and CuO_2 plane sites.

From the perspective of electronic structure: the absence of oxygen alters the local electronic structure. If we were able to observe the oxygen electron environment in YBCO, we would detect changes indicative of oxygen deficiency. As established knowledge suggests, oxygen vacancies predominantly occur at chain and plane sites. At these sites, oxygen is hybridized with copper. Consequently, when oxygen is removed, the hybridizations associated with the oxygen K-edge pre-peak diminish first. This pre-peak, which precedes the main peak, exhibits greater sensitivity to minor oxygen deficiencies compared to the main peak. Van Aken et al. performed a systematic investigation of the O K-edge EELS spectra across a wide variety of transition-metal oxides in Fig.1.6. They demonstrated that the pre-peak feature observed at around 530 eV is a direct consequence of hybridization between O 2p and unoccupied metal 3d orbitals.[44] By comparing synthetic and mineral samples, they confirmed that the pre-peak is intrinsic to metal–oxygen bonding.

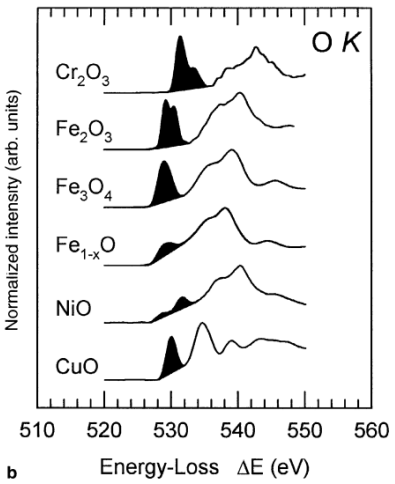

Fig .1.6. EELS O K-edge of 3d transition metal. CuO is at the bottom of the spectrum.[44]

According to this pre-peak information, researchers have started utilizing tools such as X-ray Absorption Spectroscopy (XAS) and Electron Energy-Loss Spectroscopy (EELS), which are capable of observing changes in the electron structure, to investigate oxygen deficiency in YBCO. Nücker et al. used polarization-dependent XAS to study the oxygen deficiency in YBCO.[45] In their study, they found the difference at different sites. It demonstrated that the O K-edge pre-peak at the Cu–O chain sites decreases progressively with increasing δ, with significant damping observed around $\delta \approx 0.4$. However, as we know in YBCO when δ is over 0.6, there is almost no superconducting behaviour. The sensitivity in XAS actually cannot help us to catch the small change in δ. Also in their

research, the explanation of the oxygen deficiency distribution site and T_c is rare.

Browning et al. 1992 conducted one of the earliest quantitative studies on oxygen non-stoichiometry in $YBa_2Cu_3O_{7-\delta}$ using electron energy-loss spectroscopy (EELS). Their analysis focused on the O K-edge spectrum, particularly the pre-edge feature located near 530 eV, which corresponds to transitions from O 1s to hybridized O 2p–Cu 3d states.[46] By measuring changes in the intensity of this pre-peak, they established a direct correlation with δ across a series of YBCO samples with known stoichiometry. A notable finding of their study was that in heavily deoxygenated samples (e.g., $YBa_2Cu_3O_6$), the pre-peak nearly vanished, consistent with the breakdown of Cu–O chain hybridization. Both electron energy-loss spectroscopy (EELS) and X-ray absorption spectroscopy (XAS), particularly at the O K-edge, have proven to be powerful tools for probing local oxygen deficiency and electronic structure in transition-metal oxides.

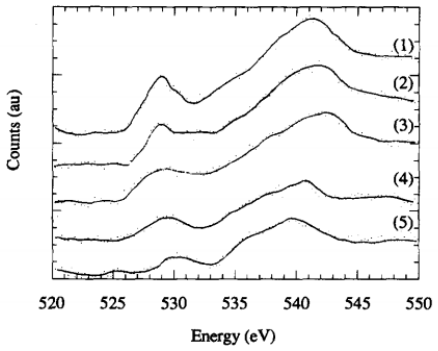

Fig 1.7 EELS of YBCO with varying δ. (1) $\delta \approx 0.1$, (2) $\delta \approx 0.2$, (3) $\delta \approx 0.3$, (4) $\delta \approx 0.4$, (5) $\delta \approx 0.5$.[46]

In summary, various techniques have been employed to investigate oxygen deficiency in YBCO, each with specific strengths and limitations. Structural methods like XRD and neutron diffraction are effective for evaluating average oxygen content and occupancy trends, but lack spatial resolution and site specificity. TEM enables high-resolution imaging of local structural features, yet it struggles to directly detect oxygen vacancies due to the low scattering cross-section of oxygen atoms. Electronic structure techniques such as XAS and EELS provide spectral fingerprints sensitive to oxygen coordination, but XAS is often limited by its poor spatial resolution and reduced sensitivity to small δ changes in lightly deoxygenated samples.

In contrast, EELS stands out as a powerful tool that overcomes many of these limitations. It offers high spatial resolution capable of probing local electronic environments and site-specific oxygen deficiency at the nano-meter scale. Moreover, its sensitivity to changes in the O K-edge pre-peak allows for direct, visualizable tracking of hybridization loss associated with oxygen vacancies—making it uniquely suited for simultaneously resolving both the location and electronic consequences of oxygen deficiency in complex oxides like YBCO.

In this context, the present study contributes a novel perspective by applying aberration-corrected STEM-EELS to directly correlate site-specific oxygen deficiencies with superconducting properties in YBCO thin films. While previous studies have used either bulk-sensitive methods (e.g., XRD, neutron diffraction) or spatially averaged spectroscopy (e.g., XAS), but they have not demonstrated the capability to resolve local electronic structure variations at individual atomic columns, especially in thin films where oxygen ordering and strain can vary on the nanometer scale. This technique allows us not only to identify where oxygen deficiencies form (chains vs. planes), but also to quantify their spectral consequences and relate them to T_c suppression in a spatially resolved manner. In doing so, this work demonstrates the technical novelty of STEM-EELS in addressing longstanding questions in high-T_c superconductivity.

1.5 Research Objectives

Building upon the limitations identified in previous studies, this research aims to elucidate the site-specific nature and spatial distribution of oxygen deficiencies in $YBa_2Cu_3O_{7-\delta}$ (YBCO) at the atomic scale, and to uncover their correlation with T_c. While the critical role of average oxygen content in tuning T_c is well-established, the influence of oxygen deficiencies at distinct crystallographic sites, particularly in Cu–O chains and

CuO_2 planes, remains unresolved due to the lack of spatially resolved techniques.

This study introduces a technically novel approach using aberration-corrected scanning transmission electron microscopy (STEM) in combination with electron energy-loss spectroscopy (EELS), enabling site-specific quantification of oxygen deficiency and its spectroscopic signatures. This high-resolution, spatially targeted method offers significant advantages over previous bulk or averaged measurements.

The specific objectives are:

- To map oxygen deficiency distributions between CuO_2 planes and Cu–O chains in YBCO thin films using STEM-EELS.
- To quantify changes in the O K-edge pre-peak associated with site-specific oxygen loss.
- To compare samples with different T_c values and assess the relationship between local oxygen deficiency and superconductivity.
- To demonstrate the feasibility and innovation of using STEM-EELS for probing local structure–property relationships in complex oxide superconductors.

By combining structural and electronic analyses at atomic resolution, this study advances both the methodology of defect characterization and the fundamental understanding of high-T_c superconductivity in nonstoichiometric cuprates.

Chapter 2.Theoretical Framework

2.1 Basics of Scanning Transmission Electron Microscopy (STEM)

2.1.1 Fundamentals and Instrumentation of STEM

Scanning Transmission Electron Microscopy (STEM) is a powerful technique that combines high spatial resolution imaging with analytical capabilities, enabling atomic-scale investigations of materials. The fundamental setup of a STEM involves focusing a convergent electron beam onto a thin specimen using a series of condenser lenses and scanning it in a raster pattern. As electrons interact with the specimen, various signals are generated—such as transmitted, scattered, and inelastically scattered electrons—which can be detected to form images or spectra.

A typical STEM column, as shown in Fig. 2.1 includes:

- **Field Emission Gun (FEG)** as a coherent electron source.
- **Condenser lenses**, which demagnify the source to produce a fine electron probe.
- **Objective lens**, which provides the final focusing step to achieve sub-angstrom resolution.
- **Scanning coils**, which deflect the beam to scan across the sample.
- **Detectors**, which collect electrons for multiple imaging modes, including Bright

Field (BF), Annular Dark Field (ADF), and High-Angle Annular Dark Field (HAADF).

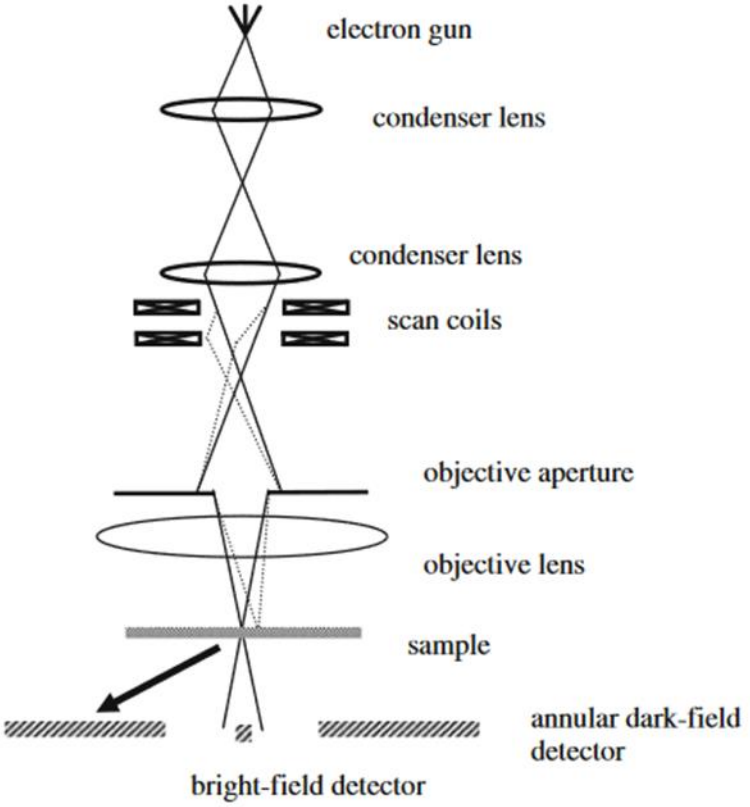

Fig.2.1 Schematic diagram of a scanning transmission electron microscope (STEM).[47]

The high-angle annular dark field (HAADF) mode is particularly useful for atomic-resolution imaging, as the detected intensity approximately scales with the square of the atomic number (Z^2), resulting in strong "Z-contrast". This incoherent imaging mode allows for straightforward interpretation of structural features without phase contrast

artifacts.

Compared to conventional TEM, STEM offers a more direct way to form high-resolution images without the need for image reconstruction via Fourier techniques. The use of an annular detector to collect only the scattered electrons at large angles greatly enhances the contrast for heavy atoms, making it especially effective in complex oxides and materials containing multiple elements.

In addition to imaging, STEM is compatible with spectroscopic methods such as EELS and Energy-Dispersive X-ray Spectroscopy (EDS), allowing simultaneous structural and chemical analysis at the atomic level. These analytical extensions make STEM a cornerstone technique in modern materials science.

2.1.2 Electron–Specimen Interaction in STEM

In scanning transmission electron microscopy (STEM), a finely focused electron probe is rastered across the sample, and the scattered electrons are collected at each probe position to generate high-resolution images. The interaction between the incident electron beam and the specimen is central to image formation and spectroscopic analysis. As electrons penetrate the sample, they undergo both elastic and inelastic scattering events. Elastic scattering, which preserves the energy of the electrons, is responsible for contrast

mechanisms such as phase contrast and diffraction. In contrast, inelastic scattering involves energy transfer from the electrons to the specimen, giving rise to signals used in spectroscopies like electron energy-loss spectroscopy (EELS).

The electron-specimen interaction depends on several factors: the beam energy, the thickness and composition of the sample, and the local atomic number (Z). High-Z atoms tend to scatter electrons more strongly, particularly at high angles, which forms the basis of Z-contrast imaging in high-angle annular dark-field (HAADF) STEM. Moreover, thermal diffuse scattering (TDS), arising from atomic vibrations, dominates image contrast at high scattering angles when the inner angle of the detector is chosen appropriately. This incoherent scattering mechanism ensures that HAADF images are largely free from interference effects and can be directly interpreted as maps of atomic number and specimen thickness.

The STEM probe's interaction volume is relatively confined compared to conventional TEM due to the narrow convergence angle and small probe size, enabling sub-ångström resolution. However, this also introduces sensitivity to probe-specimen alignment, particularly when imaging crystalline materials along specific zone axes. Beam channelling and delocalization can occur under such conditions, affecting the spatial localization of signals. Therefore, understanding the electron–specimen interaction is

crucial for optimizing imaging conditions and accurately interpreting structural and spectroscopic information.

2.1.3 Ronchigram and Its Role in Aberration Correction

In practical STEM operation, acquiring a **Ronchigram** is often the first step before collecting high-resolution images. Microscopists use it to assess the beam condition: when the Ronchigram appears symmetric and clean, the resulting atomic-resolution images are significantly sharper and more interpretable. This seemingly simple observation—that "tuning the Ronchigram leads to clearer pictures"—has a solid physical foundation rooted in the wave optics of electron beams.

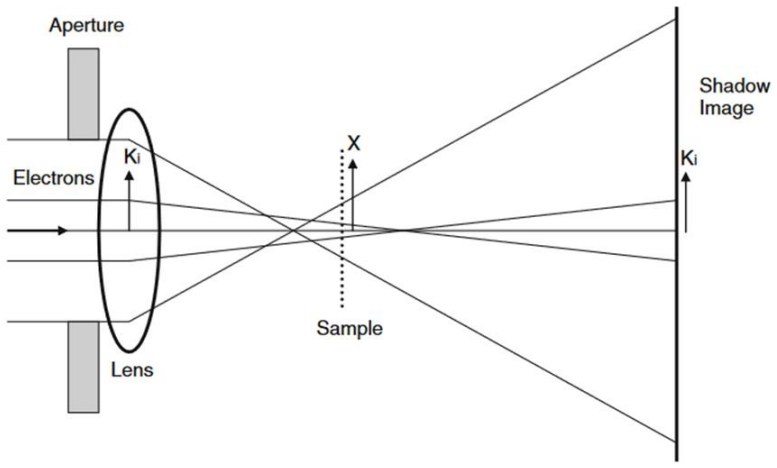

Fig.2.2 Geometrical interpretation of Ronchigram formation in STEM.[47]

This schematic illustrates the basic optical path for Ronchigram generation. A convergent electron beam passes through an aperture and is focused by the lens to the sample plane. When the probe is slightly defocused, electrons scattered by the sample produce a shadow image pattern—known as the Ronchigram—on the detector plane. The observed contrast arises from phase shifts in the wavefront, induced by aberrations in the lens system and local potential gradients within the specimen. This image is used for alignment and aberration correction to achieve optimal probe shape and resolution.

A Ronchigram is formed when a convergent electron probe passes through a thin sample, and the transmitted beam is projected onto a detector plane at or near the defocus condition. The pattern reveals how the electron wavefront interacts with the local potential of the specimen and how it has been distorted by residual lens aberrations such as defocus, astigmatism, or coma. When these aberrations are present, the wavefront becomes warped, leading to curved fringes, asymmetry, or localized distortions in the Ronchigram image.

As illustrated in Fig 2.2, the Ronchigram can be understood in the geometrical optics framework as a shadow image of the sample's interaction with the electron probe. Rays that would otherwise travel in straight paths are deflected by local phase gradients introduced by lens imperfections. The central region of the Ronchigram is especially

sensitive to low-order aberrations: when it appears flat and uniform, it indicates minimal wavefront curvature, meaning the probe is near its ideal focus.

From a wave-optical perspective, the Ronchigram is effectively a real-space interference pattern created by overlapping electron waves. Aberrations deform the shape and symmetry of these wavefronts, leading to predictable and interpretable distortions in the image. By iteratively adjusting correctors to minimize these distortions—either manually or via auto-correction software—users can refine the shape of the probe.

This optimization has a direct consequence on image quality: a well-corrected Ronchigram corresponds to a tightly focused, nearly aberration-free probe, which increases both the lateral resolution and the signal-to-noise ratio in high-angle annular dark-field (HAADF) imaging and spectroscopic techniques such as EELS. Especially for beam-sensitive samples or atomic-scale structural analysis, this preliminary tuning step is critical.

In summary, the Ronchigram serves as a visual diagnostic of probe quality. Correcting it improves image sharpness not by adjusting the sample, but by shaping the electron beam into its most coherent and localized form. It bridges practical imaging with fundamental wave optics and remains an essential step in high-resolution STEM workflows.

2.1.4 High-Angle Annular Dark Field (HAADF) Imaging

In scanning transmission electron microscopy (STEM), the spatial distribution of scattered electrons carries rich information about the atomic structure and composition of the sample. By placing detectors at different angular positions beneath the specimen, one can collect specific subsets of scattered electrons, resulting in various imaging modes—each emphasizing different physical interactions.

As illustrated in Fig 2.1, the STEM setup includes a highly focused electron beam generated by the electron gun and condenser lens system. The beam is scanned over the sample using electromagnetic coils. Upon interacting with the specimen, electrons are scattered to a wide range of angles depending on atomic number, local thickness, and bonding environment. These scattered electrons are selectively captured by detectors positioned beneath the sample.

The bright-field (BF) detector collects unscattered or low-angle elastically scattered electrons using an on-axis detector. This imaging mode is often sensitive to diffraction contrast and phase interference, which makes interpretation challenging, especially in thicker or multi-element samples.

In contrast, annular dark-field (ADF) imaging collects electrons scattered to

intermediate and high angles using an annular detector. ADF imaging reduces the influence of diffraction and provides enhanced contrast for heavier elements. It offers more direct visualization of structural features, although contrast interpretation can still depend on diffraction conditions and sample orientation.

When the inner angle of the ADF detector is increased further—typically beyond 50–70 milliradians, the system operates in the high-angle annular dark field (HAADF) regime. In this configuration, the detected signal arises primarily from incoherent elastic scattering and thermal diffuse scattering (TDS), both of which are localized interactions. This makes HAADF images insensitive to defocus, interference fringes, or dynamical diffraction effects.

A key advantage of HAADF imaging is its strong dependence on atomic number. Because high-angle scattering cross-sections scale approximately with the square of the atomic number (Z^2), HAADF images exhibit Z-contrast: heavier elements appear brighter than lighter ones. This allows for intuitive interpretation of composition and atomic arrangement, even in complex oxides or heterostructures.

To optimize HAADF image quality, several conditions must be satisfied:

The detector inner angle should be sufficiently high to suppress Bragg diffraction and capture predominantly incoherent scattering.

The electron probe must be well-focused and aberration-corrected (see Section 2.1.3 on Ronchigram adjustment).

The sample should be thin enough to minimize multiple scattering while still generating sufficient signal.

Because of its robustness, elemental sensitivity, and ease of interpretation, HAADF imaging is widely used as a structural reference in correlative analyses involving spectroscopic techniques such as electron energy-loss spectroscopy (EELS) or energy-dispersive X-ray spectroscopy (EDX). In this work, HAADF images are employed to guide spatially resolved EELS acquisition and to correlate structural features with site-specific oxygen deficiencies in $YBa_2Cu_3O_{7-\delta}$.

2.2 Basics of Electron Energy Loss Spectroscopy (EELS)

2.2.1 Fundamentals of EELS and Energy-Loss Mechanisms

Electron Energy-Loss Spectroscopy (EELS) analyzes how fast electrons lose energy as they pass through a thin sample and interact with the atoms in the material. These energy losses occur via inelastic scattering events, where the incident electron transfers a portion of its kinetic energy to the sample. The lost energy corresponds to specific excitations within the material and thus reveals rich information about the local electronic structure,

chemical composition, and bonding environment.

In essence, the energy loss of the electron reflects the energy it used to “do something” inside the sample. These “interactions” include the following types:

- **Exciting valence electrons:**

The fast electron may excite loosely bound valence electrons (e.g., in the conduction band), promoting them to higher unoccupied states. This process typically occurs at low energy loss (a few eV to tens of eV), contributing to features such as interband transitions and plasmon peaks.

- **Ionizing core electrons (inner-shell excitation):**

At higher energy losses (typically above 50 eV), the incident electron has sufficient energy to eject tightly bound core-level electrons (e.g., O 1s, Cu 2p) from atoms in the material. This process creates a core hole and leaves the atom in an excited state. The energy required for this transition appears as a sharp ionization edge in the EELS spectrum. Because each element has a unique core binding energy, these edges serve as fingerprints for elemental identification.r

- **Exciting collective oscillations (plasmons):**

In conductive materials, electrons can collectively oscillate as a group. The fast electron may lose energy by exciting such plasmons—coherent oscillations of the electron

gas—resulting in distinct low-loss peaks.

Coupling with phonons or lattice vibrations (in low-energy regions, typically < 1 eV in monochromated systems): The electron may also lose energy by transferring a small amount of energy to the lattice, initiating phonon excitations. Thus, every energy loss peak in the EELS spectrum corresponds to a specific interaction mechanism—a "transaction" in which the electron pays a defined amount of energy to trigger an internal excitation in the material. The spectrometer records how much energy the electron lost, and this information tells us what process occurred. These processes are all non-elastic, meaning the incident electron emerges with less energy than it had before the interaction. In contrast, elastically scattered electrons undergo deflection without energy change and are used in diffraction-based imaging, not in EELS.

Before exploring inelastic signals, it is important to understand the role of the zero-loss peak (ZLP), which serves as the foundation for energy calibration.

In a typical EELS spectrum, the zero-loss peak (ZLP) is the most prominent feature, located at 0 eV energy loss. It corresponds to those electrons that have passed through the specimen without undergoing any inelastic scattering, they retain their original kinetic energy. Although not part of the inelastic loss signal itself, the ZLP serves multiple critical functions: It acts as an energy reference, anchoring the zero point for subsequent energy-

loss measurements. Its full width at half maximum (FWHM) is a direct indicator of the energy resolution of the instrument, determined by the electron source, monochromator, and spectrometer dispersion. Its intensity relative to the rest of the spectrum provides a rough estimate of sample thickness via the log-ratio method, as thicker specimens reduce the relative height of the ZLP due to increased inelastic scattering.

During background subtraction, especially near core-loss edges, the long tail of the ZLP may overlap with edge onsets and must be carefully modeled or deconvolved to ensure accurate edge analysis.

In energy-filtered TEM (EFTEM) and monochromated EELS applications, the ZLP is also used to track and correct for instrumental drift and energy shifts over time. In this study, the ZLP was used to calibrate the energy axis and to assess the beam stability prior to core-loss acquisition.

The EELS spectrum is broadly divided into two regions:

- **Low-Loss Region (0–50 eV):**

Includes energy losses due to plasmon excitations, interband transitions, and surface effects. This region is useful for estimating thickness, bandgap features, and collective behavior of electrons.

- **Core-Loss Region (>50 eV)**:

Arises from ionization of inner-shell electrons. The resulting edges (e.g., O K-edge, Cu L-edge) provide element-specific and chemically sensitive information, including oxidation states and coordination environments.

Because these scattering events occur within a nanometer-scale interaction volume, and because only electrons that have undergone energy loss are analyzed, EELS enables spatially resolved spectroscopic analysis when combined with STEM. This allows mapping of chemical and electronic variations at interfaces, grain boundaries, and defect sites with atomic precision.

2.2.2 Core-Loss Region and Fine Structures

The core-loss region of an EELS spectrum corresponds to energy losses that are large enough to excite tightly bound core-level electrons from inner atomic shells (such as 1s, 2p, or 3d) into unoccupied higher-energy states. These transitions give rise to sharp ionization edges, which mark the energy threshold required to remove an electron from a specific core orbital of a given element.

Each element has a unique set of binding energies, and thus a unique position of its ionization edges. For example:

- The O K-edge (typically near 530 eV) arises from the excitation of O 1s electrons;

- The Cu $L_{2,3}$-edges (near 930–950 eV) originate from transitions of Cu 2p electrons;
- The Ba M-edge involves transitions from Ba 3d orbitals.

Because of this element-specific nature, core-loss edges serve as spectroscopic fingerprints, enabling precise elemental identification. However, beyond simple detection, the fine structure near the onset of these edges provides a wealth of additional chemical and electronic information. Immediately following the onset of a core-loss edge, the spectrum often exhibits oscillations, peaks, or shoulders that result from the interaction between the excited electron and the local electronic environment. This portion is referred to as the Energy-Loss Near-Edge Structure (ELNES).

The shape and intensity of the ELNES features are sensitive to:

- Oxidation state:

A higher oxidation state typically shifts the ionization edge to higher energies, and changes the occupancy of final states, thereby altering the pre-edge or white-line intensity.

- Local coordination and symmetry:

The geometry of neighboring atoms—such as tetrahedral vs. octahedral coordination—can split the density of unoccupied states (due to ligand field effects), resulting in multiple peaks or shoulders in the edge.

- Bonding character and hybridization:

ELNES reflects the partial density of unoccupied states available to the excited electron. Covalent bonding, orbital hybridization, and even crystal field effects contribute to the formation and shape of these features.

These characteristics make ELNES an essential tool for probing local bonding environments, valence state variations, and electronic structure differences at the nanoscale.

In some edges—especially the O K-edge—a weak peak may appear just before the main rise of the ionization edge. This pre-edge arises from transitions to low-lying unoccupied states just above the Fermi level, such as hybridized metal–oxygen orbitals or localized defect states. The presence, intensity, and energy position of the pre-edge are often indicative of:

- Degree of hybridization (e.g., Cu 3d–O 2p),
- Oxygen vacancy concentration,
- Carrier density in p-type or n-type materials.

Because pre-edge features are typically weak and narrow, their detection requires high energy resolution and careful spectral background subtraction.

Together, the ionization edge onset, ELNES, and pre-edge structure form a comprehensive fingerprint of the chemical and electronic identity of atoms in a material.

When acquired with high spatial resolution in STEM mode, these features can be mapped across individual atomic columns or defect sites, providing unmatched insight into site-specific oxidation states, coordination changes, and oxygen deficiency, as will be shown in later chapters of this dissertation.

2.2.3 Advantages and Spatial Resolution in STEM-EELS

When integrated into a scanning transmission electron microscope (STEM), EELS becomes an exceptionally powerful tool for spatially resolved chemical and electronic analysis. Its most notable advantage lies in its ability to combine elemental sensitivity, electronic structure resolution, and atomic-scale spatial precision in a single experimental setup.

In STEM-EELS, the electron probe can be focused to a sub-angstrom diameter and rastered across the sample with high positional control. At each pixel of the scanned region, an EELS spectrum is acquired, producing a spectrum image (SI)—a data cube that contains both structural and spectroscopic information at nanometer or even atomic resolution.

This allows direct mapping of:

- Elemental distributions across interfaces, grain boundaries, and point defects,

- Local variations in oxidation states or coordination environments,
- Spatial distribution of oxygen vacancies, especially when analyzing core-loss edge fine structures.

Such spatial resolution is unattainable in conventional bulk-averaged techniques like X-ray Absorption Spectroscopy (XAS). While XAS provides valuable information on electronic transitions and local coordination, it typically averages signals over areas ranging from micrometers to millimeters, making it blind to nanoscale inhomogeneities that critically affect functional properties in complex oxides.

Both EELS and XAS probe unoccupied electronic states by exciting core electrons and analyzing the transition probability into higher energy levels. In this sense, their spectral features—especially near-edge fine structures—are physically analogous. However, there are key distinctions:

Table 2.1 Comparison between STEM-EELS and XAS

Feature	**STEM-EELS**	**XAS**
Spatial resolution	Sub-nanometer to atomic	> μm (typically bulk-averaged)
Beam source	Electron beam	Synchrotron X-rays
Sample requirements	Thin lamella (~10–100 nm)	Bulk or thin films
Sensitivity to oxygen deficiency	High (through O K-edge pre-peak)	Moderate, but spatially averaged

In short, EELS retains many of the chemical and electronic sensitivities of XAS, but offers the added benefit of high spatial selectivity, co-registration with atomic structure, and compatibility with in situ conditions.

Suitability for Oxygen Deficiency Analysis in YBCO

In the context of this study, STEM-EELS is particularly well-suited to probe site-specific oxygen deficiency in YBCO. The following advantages are critical:

The O K-edge pre-peak intensity and shape provide a sensitive indicator of local oxygen coordination and valence state changes.

The technique allows distinguishing between different oxygen sublattices (e.g., chain vs. plane sites) within a single unit cell.

Spectrum imaging combined with HAADF-STEM ensures precise alignment between chemical signal and atomic structure.

For these reasons, this work adopts atomic-resolution STEM-EELS as the primary characterization method to map the spatial evolution of oxygen content and correlate it with superconducting behavior.

Chapter 3 Experimental Methods

3.1 Fabrication and Oxygen Control of YBCO Thin Films

Thin films of $YBa_2Cu_3O_{7-\delta}$ (YBCO) were fabricated on single-crystalline $LaAlO_3$ (001) substrates using pulsed laser deposition (PLD). This method offers precise control over film thickness and stoichiometry, which is essential for systematic investigation of oxygen-deficiency-dependent phenomena. The deposition process was conducted at a substrate temperature of 800 °C under an oxygen partial pressure of 30 Pa. The laser fluence was maintained at 250 mJ per pulse, with a target-to-substrate distance of 4.5 cm. These parameters were selected based on prior optimization to ensure uniform growth and good epitaxial quality.

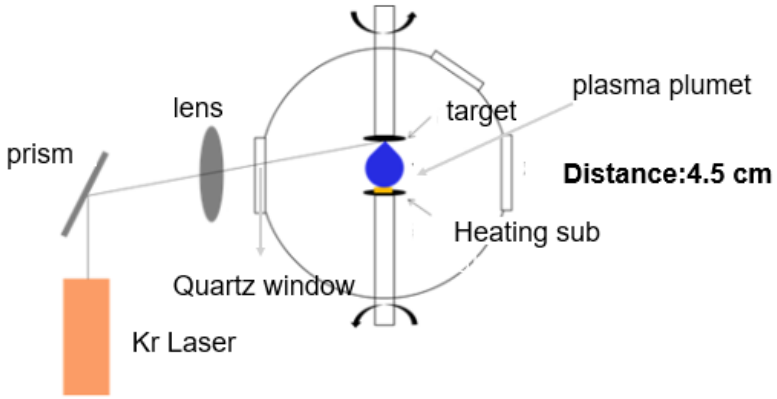

Fig.3.1 Basic structure diagram of pulse laser deposition system

The as-grown YBCO films typically exhibit oxygen non-stoichiometry due to insufficient incorporation of oxygen during the low-pressure deposition process. These films did not exhibit superconductivity, as confirmed by electrical transport measurements, and are characterized by a high density of oxygen vacancies.

To systematically tune the oxygen content and investigate its influence on superconducting properties, post-deposition oxygen annealing was performed under controlled conditions. Two different annealing environments were employed:

In-situ annealing in the PLD chamber at 480 °C under 30 Pa oxygen for 10 and 30 minutes; Ex-situ annealing in a standard tube furnace at 480 °C under 1 atm oxygen for 10 and 30 minutes.

Due to hardware constraints, high-pressure oxygen annealing (>100 Pa) could not be performed in the PLD chamber without risking thermal damage to internal components. The detailed oxygen treatment conditions and corresponding superconducting T_c are summarized in Table 3.1. T_c values, determined from resistance–temperature (R–T) measurements, ranged from approximately 49 K to 86 K.

Table 3.1. Oxygen treatment parameter of YBCO samples

T_c (K)	Oxygen treatment temperature	Oxygen pressure (Pa)	Oxygen treatment time
49	480	30	10
64	480	30	30
83	480	1atm	10
86	480	1atm	30

X-ray diffraction (XRD) was used to assess the crystal quality and phase composition of the films. Measurements were performed using a Cu Kα source (λ = 1.5406 Å) operated at 40 kV and 30 mA. A monochromator was employed to enhance spectral resolution and reduce background noise. The scan range for θ–2θ measurements was 30° to 90°, with a step size of 0.01°, and a slit configuration of 1° (divergence), 1° (scattering), and 0.2 mm (receiving).

3.1.1 Rationale for Using Thin Films Instead of Bulk Single Crystals

In this study, pulsed laser deposition (PLD) was employed to fabricate epitaxial $YBa_2Cu_3O_{7-\delta}$ (YBCO) thin films rather than bulk single crystals. This choice was motivated by several practical and technical considerations. First, thin films enable precise control of oxygen content via post-annealing under tunable pressure and temperature conditions, allowing us to systematically obtain samples with different T_c from a single target composition. Second, thin films are more compatible with high-

resolution STEM and EELS, as they can be readily thinned to electron transparency and are free from cleavage-induced damage or surface charging, which are common issues in bulk specimens.

While it is true that lattice constants in thin films may be affected by substrate-induced strain or lattice relaxation near interfaces. But we will get the HAADF image of the observation area first to check the crystalline. These observations (in Chapter 4) suggest that the analyzed region is structurally relaxed and can reasonably represent the intrinsic properties of the film. Furthermore, as discussed in Chapter 4, although the c-axis variation with T_c is smaller than that observed in bulk crystals, our experimental trend is consistent with literature reports on thin-film YBCO systems. Thus, despite these challenges, thin films provide a reliable and reproducible platform for investigating the atomic-scale correlation between oxygen non-stoichiometry and superconductivity.

In addition, thin-film YBCO is of great practical importance, as it is widely used in the fabrication of superconducting devices such as SQUIDs, Josephson junctions, and microwave filters. Therefore, studying oxygen deficiencies and their influence on Tc in thin films not only advances fundamental understanding but also lays a foundation for improving the performance and stability of high-T_c superconducting electronics.

3.2 Preparation of Cross-Sectional STEM Specimens

To prepare high-quality cross-sectional specimens of $YBa_2Cu_3O_{7-\delta}$ (YBCO) thin films suitable for atomic-resolution STEM-EELS analysis, a two-step thinning process was employed: coarse milling using focused ion beam (FIB) followed by low-damage polishing with argon ion milling.

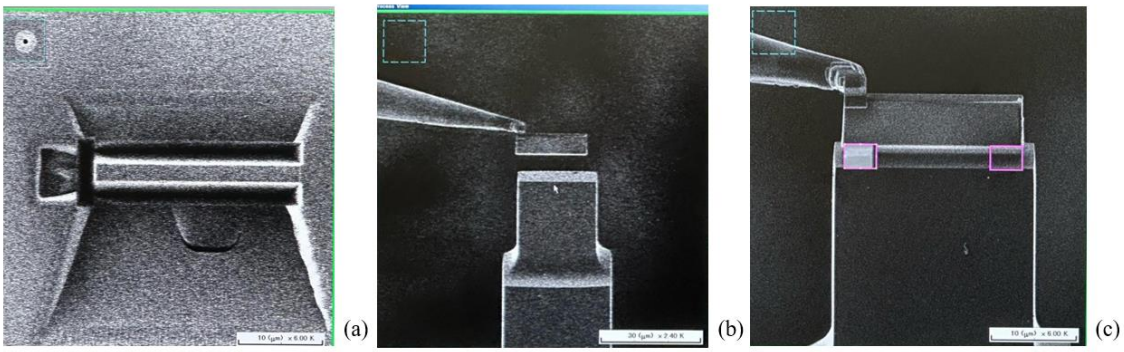

Fig 3.2.FIB process for specimen thinning.

As illustrated in Fig 3.2, the FIB-based specimen preparation was conducted using an SMI3050 system (SII NanoTechnology). The process involved: (a)Defining a region and thinning the sample to several hundred nanometers by gallium ion milling;(b) Picking up the thinned lamella using the probe; (c) Attaching and securing the lamella onto a Mo TEM grid using W deposition.

The step-by-step operation is shown in Fig 3.2 (a–c). Throughout the process, a

scanning ion microscopy (SIM) mode was used to monitor sample quality in real time.

However, FIB milling typically introduces surface amorphization and ion implantation damage, particularly on the outermost atomic layers. To minimize these effects, a final low-voltage polishing step was performed using a Gentle Mill system (Technology Linda). The pre-mounted specimens were irradiated with low-energy Ar^+ ions (<1 kV) under a broad beam, gradually removing the damaged surface layers and reducing the overall thickness to <100 nm. This post-processing step was essential for ensuring both beam transparency and spectral fidelity in subsequent STEM-EELS experiments.

This combined preparation protocol—FIB-assisted lift-out and low-energy Ar ion milling—ensures atomic-level cleanliness and stability under the electron beam, which is especially important when analyzing beam-sensitive oxides such as YBCO.

To ensure optimal sample thickness, we adopted a trial-and-error approach. After the initial gentle milling process, the thickness of each specimen was checked using conventional TEM imaging. If the measured thickness exceeded 100 nm, additional gentle milling was applied. However, in subsequent thinning cycles, the milling duration was carefully reduced to prevent sample breakage. This iterative refinement ensured the preparation of high-quality lamellae suitable for atomic-resolution analysis.

3.3 Experimental Setup for STEM-EELS Analysis

High-resolution scanning transmission electron microscopy (STEM) imaging and electron energy-loss spectroscopy (EELS) measurements were carried out using a JEOL ARM-200F transmission electron microscope. The instrument was operated at an accelerating voltage of 200 kV and was equipped with a thermal field emission gun and a spherical aberration (Cs) corrector for the illumination system. These features enabled the formation of a sub-angstrom electron probe, providing the spatial resolution required for atomic-scale compositional and electronic structure mapping.

A convergence semi-angle of approximately 23 mrad was employed to ensure optimal spatial resolution while maintaining sufficient beam current for EELS acquisition. The probe current was maintained at around 10 pA to balance signal quality with beam-induced damage suppression—particularly important for the oxygen-sensitive YBCO system.

High-angle annular dark-field (HAADF) images were acquired simultaneously with EELS data to provide structural context. The inner and outer collection semi-angles were set to 70 mrad and 170 mrad, respectively. This configuration enhances Z-contrast and allows for reliable visualization of atomic columns corresponding to heavy and light

elements.

EELS measurements were performed using a Gatan GIF Quantum energy filter installed on the microscope. The EELS spectra were acquired with the following settings:

- Collection semi-angle: 20 mrad
- Energy dispersion: 0.1 eV/channel
- Energy resolution: ~1 eV, as determined by the full width at half maximum (FWHM) of the zero-loss peak (ZLP)

Each spectrum was energy-calibrated by referencing the position of the ZLP prior to core-loss acquisition. To suppress high-frequency noise while preserving the spectral fine structure, the recorded spectra were smoothed using a Gaussian filter with a standard deviation of $\sigma = 0.2$ eV. This filter width was carefully selected to avoid artificial broadening of key features such as the pre-peak of the oxygen K-edge.

All STEM-EELS data were acquired at room temperature under static vacuum conditions. Spectrum images (SIs) were collected by rastering the probe over the region of interest and acquiring a full EELS spectrum at each pixel. The spatial resolution of the SIs was matched to the HAADF image to allow for direct correlation between structural features and local chemical composition.

Prior to data acquisition, Ronchigram-based aberration correction was performed to

ensure probe quality and minimize delocalization. Zero-loss peak monitoring was continuously used to assess beam stability during experiments.

This setup enabled the spatially resolved investigation of oxygen deficiencies in YBCO at atomic resolution, laying the foundation for quantitative comparison of site-specific variations in the O K-edge fine structure and their correlation with local electronic environments and superconducting behavior.

3.4 Methodology for Mapping Oxygen Deficiencies

To quantitatively analyze the spatial distribution of oxygen deficiencies in $YBa_2Cu_3O_{7-\delta}$ (YBCO), we employed atomic-resolution scanning transmission electron microscopy combined with electron energy-loss spectroscopy (STEM-EELS). The primary focus was on the oxygen K-edge (~530 eV), whose fine structure provides sensitive insight into local bonding, hybridization, and oxygen stoichiometry.

3.4.1 Spectrum Image Acquisition

EELS spectrum images (SIs) were collected in regions previously identified by high-angle annular dark field (HAADF) STEM imaging. The spatial resolution of the SIs was matched to the HAADF lattice contrast (typically ~0.1–0.2 nm per pixel) to enable atomic-column-level analysis. A full EELS spectrum was recorded at each probe position,

producing a three-dimensional dataset (x, y, energy). To minimize beam damage during data acquisition, the probe current was held below 10 pA and the exposure time was optimized to ensure sufficient signal-to-noise ratio (SNR).

3.4.2 Preprocessing and Denoising

Prior to analysis, raw EELS spectra were preprocessed to remove noise and background artifacts:

- **Energy calibration** was performed using the position of the zero-loss peak (ZLP), which was aligned to 0 eV.
- **Gaussian smoothing** was applied using a filter with $\sigma = 0.2$ eV (equivalent to 2 channels with a dispersion of 0.1 eV/channel), to reduce statistical noise while preserving peak shape and edge features.
- **Background subtraction** was carried out using a power-law fit over a pre-edge energy window (typically 480-500 eV), and extrapolated under the oxygen K-edge.

3.4.3 Pre-Peak Integration for δ Mapping

The oxygen K-edge spectra were analyzed with a focus on the **pre-peak feature** (~530 eV), which corresponds to transitions into hybridized O 2p–Cu 3d states. The integrated intensity in this range is known to correlate with the local oxygen content and

hole doping level.

3.4.4 Spatial Correlation with Structural Features

Each oxygen map was overlaid with the simultaneously acquired HAADF image to correlate the local δ value with atomic sites. Specific structural units—CuO_2 planes, Cu–O chains, BaO layers—were manually or automatically segmented using lattice periodicity and intensity profiles in HAADF contrast in Fig 3.3.

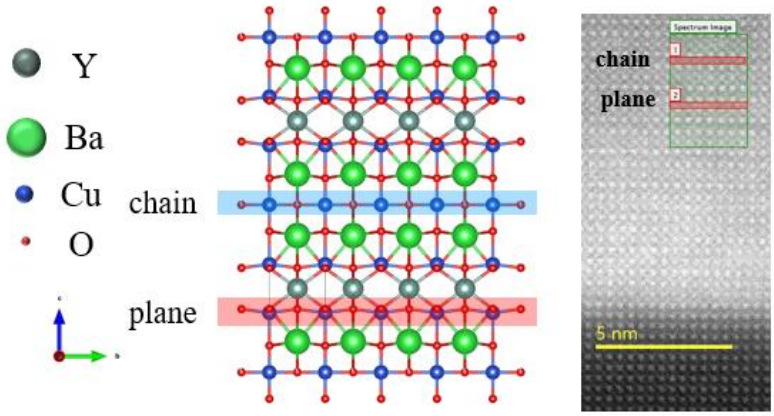

Fig 3.3 The ADF image of YBCO with the $T_c \approx 64K$. The green rectangle shows the EELS mapping area. The red rectangle shows the part which has been used for the EELS spectrum. (Left is the structure model of $YBa_2Cu_3O_7$ viewed from the [010] direction. It is constructed by stacking.)

In-plane and chain positions were assigned based on the known YBCO unit cell

structure. Averaged line profiles were extracted across targeted atomic columns to compare δ variations.

3.4.5 Quantification Strategy and Limitations

Although EELS does not directly measure oxygen atom counts, the pre-peak intensity has been widely used as a proxy for local δ when calibrated against reference samples or complementary techniques (stoichiometric standards).

In this study, we focused on relative changes in δ across atomic sites within the same field of view, rather than absolute quantification. This approach minimizes systematic errors from sample thickness, detector gain, or beam drift.

To enhance the transparency and reproducibility of our spectroscopic analysis, this section provides a detailed illustration of the raw EELS data processing procedure using the YBCO sample with a superconducting transition temperature of 64 K as a representative example. The process includes site selection, zero-loss peak calibration, background subtraction, and visualization of the unprocessed spectrum.

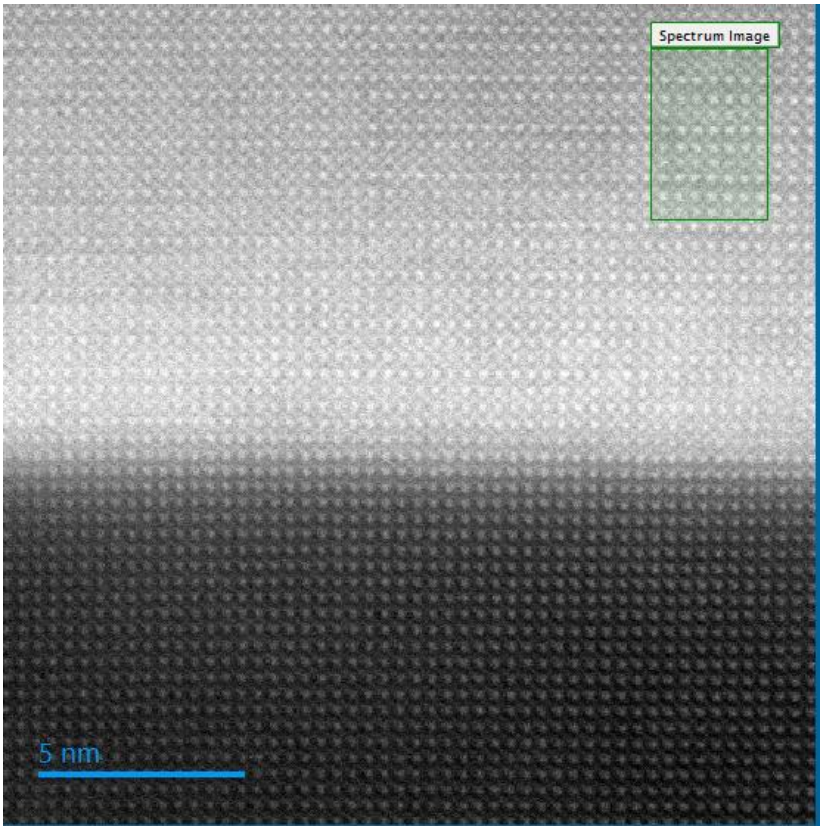

Fig. 3.4. HAADF-STEM image of YBCO thin film with a superconducting transition temperature of 64 K. The rectangular area outlined in green indicates the region selected for spectrum image (SI) acquisition.

(a) Spectrum image and site selection:

As shown in Fig. 3.4 and 3.5, a rectangular region encompassing both Cu–O chains and CuO_2 planes was selected from the HAADF image for spectrum image (SI) acquisition. The field of view covers several unit cells with clear Z-contrast. Two red

boxes (labelled 1 and 2) were drawn to extract averaged spectra from two distinct sites.

Label 1 corresponds to the Cu–O chain site,

Label 2 corresponds to the CuO_2 plane site.

These selections ensured spatial correlation with the underlying lattice structure and minimized drift artifacts.

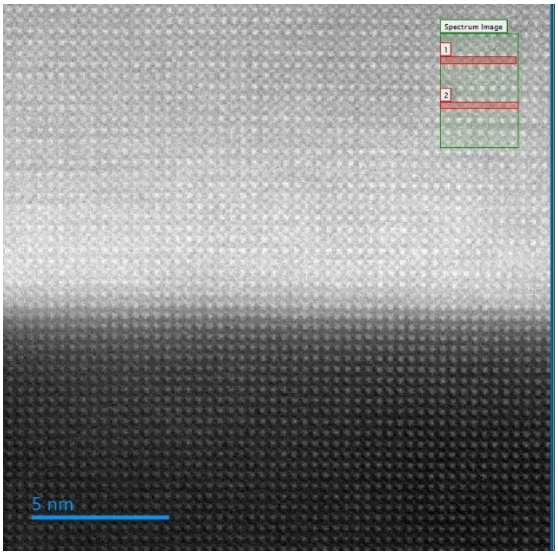

Fig 3.5 HAADF-STEM image from the Cu–O chain site in YBCO (T_c = 64 K) overlaid with EELS extraction boxes. Region 1 corresponds to the Cu–O chain site, and Region 2 corresponds to the CuO_2 plane site. These areas were selected to extract averaged O K-edge spectra from chemically distinct sites.

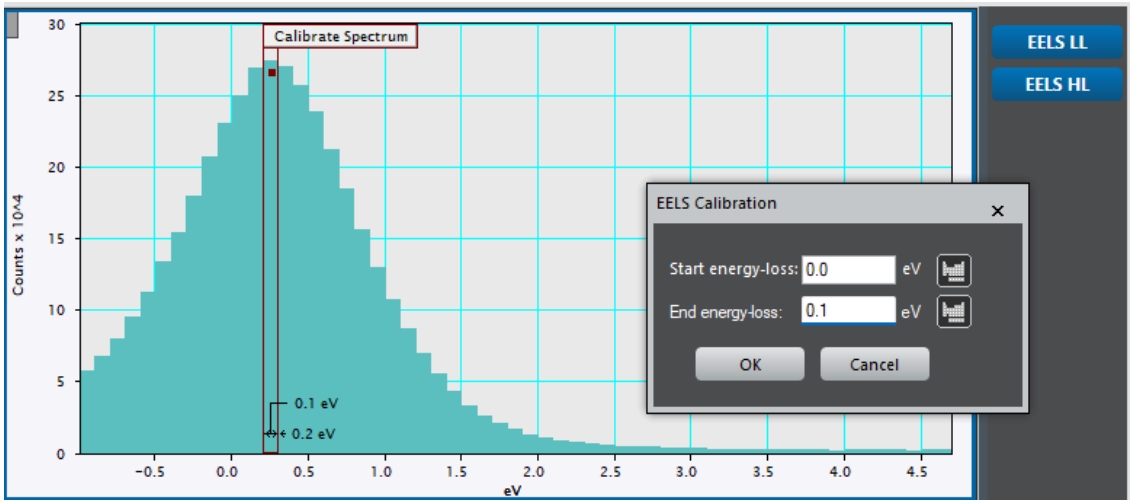

Fig. 3.6 Energy calibration of the EELS spectrum from the Cu–O chain site in YBCO (T_c = 64 K) using the zero-loss peak (ZLP). The ZLP is aligned to 0.0 eV based on a reference window between 0.0 and 0.1 eV. Accurate ZLP alignment is essential for consistent comparison of spectral features across datasets.

(b) Energy axis calibration using zero-loss peak (ZLP):

Before analyzing the core-loss region, energy calibration was performed by aligning the zero-loss peak to 0 eV. As shown in Fig. 3.6, the ZLP was centered using a linear calibration window (typically 0.0–0.1 eV). This step establishes a consistent energy reference across datasets and ensures that the O K-edge onset (~528–532 eV) is accurately aligned.

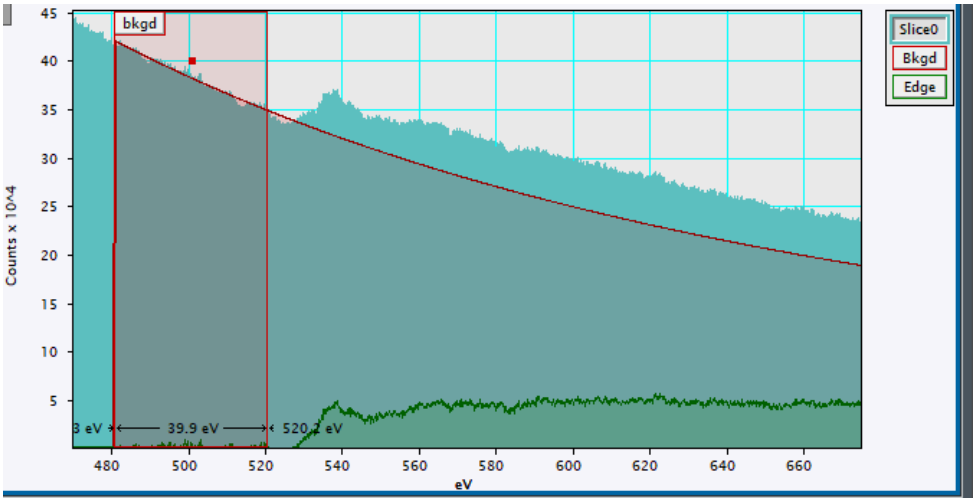

Fig. 3.7. Background subtraction of the raw O K-edge spectrum from the Cu–O chain site in YBCO (T_c = 64 K). A power-law function is fitted to the pre-edge region (typically 480–520 eV) and extrapolated beneath the ionization edge. The red curve represents the fitted background.

(c) Background subtraction:

To isolate the core-loss signal, a power-law background was fitted in the pre-edge region (e.g., 480–520 eV) and extrapolated beneath the O K-edge, as shown in Fig. 3.7 The fitted curve was then subtracted from the raw spectrum to eliminate inelastic scattering contributions unrelated to core-level excitations.

(d) Visualization of unsmoothed EELS spectra:

Fig. 3.8 shows the unsmoothed O K-edge spectrum obtained from the Cu–O chain region (T_c = 64 K). Without applying any Gaussian filtering, the spectrum exhibits evident fine structures and noise fluctuations. The pre-peak near 530 eV—attributed to hybridized Cu 3d–O 2p states—is visible but suppressed, indicating partial oxygen deficiency in the Cu–O chain.

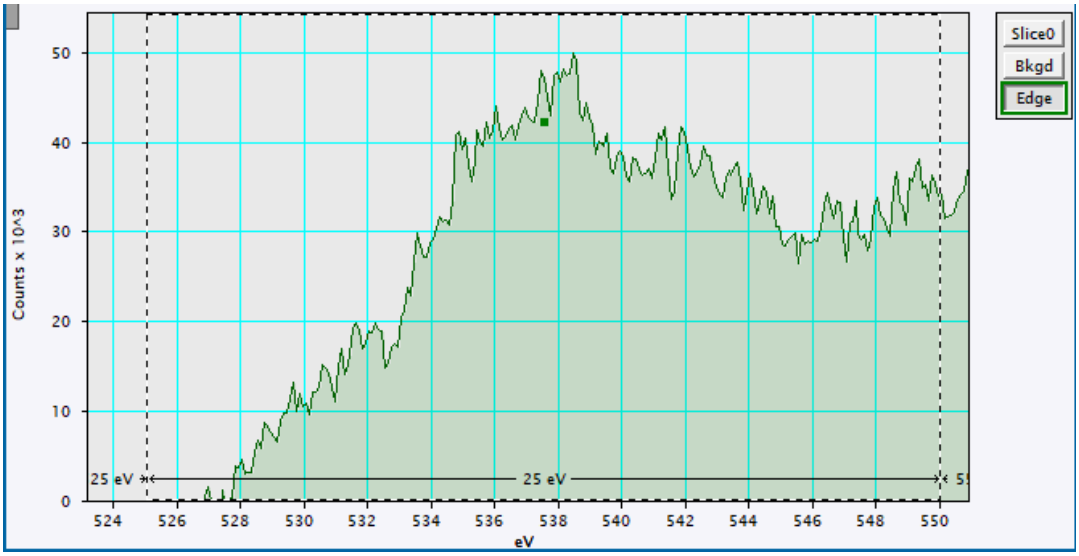

Fig. 3.8. Unprocessed O K-edge spectrum from the Cu–O chain site in YBCO (T_c = 64 K). No smoothing or denoising has been applied. The pre-peak around 530 eV appears suppressed, indicating reduced Cu–O hybridization due to oxygen deficiency.

This example highlights the full preprocessing pathway prior to the application of Gaussian smoothing ($\sigma = 0.2$ eV) and subsequent quantitative comparisons. Including such raw data examples adds rigor to the analysis and offers a benchmark for future studies using similar STEM-EELS workflows.

Chapter 4 Atomic-Scale Characterization of Oxygen Deficiency in YBCO Thin Films

4.1 Structural Characterization by XRD and STEM Imaging

To investigate the correlation between oxygen deficiency and structural features of YBCO thin films, we conducted both X-ray diffraction (XRD) and high-angle annular dark-field scanning transmission electron microscopy (HAADF-STEM) imaging. These complementary techniques allow for the examination of global crystallinity and local atomic structure, respectively.

4.1.1 X-ray Diffraction (XRD) Analysis

The periodicities parallel to the YBCO film surface were examined using the standard θ–2θ XRD method, as shown in Fig. 4.1 All samples, including the as-grown YBCO and the post-annealed films with T_c of approximately 49 K, 64 K, 81 K, and 86 K, exhibited clear diffraction peaks corresponding to the (003), (005), and (006) planes of orthorhombic $YBa_2Cu_3O_{7-\delta}$. These peaks were observed near $2\theta \approx 22.8°$, 38.0°, and 45.6°, consistent with prior reports using Cu Kα radiation. Notably, the (004) reflection was not detected, in line with theoretical intensity predictions. No significant peak shift was observed after oxygen treatments, indicating minimal changes in lattice spacing across

all samples.

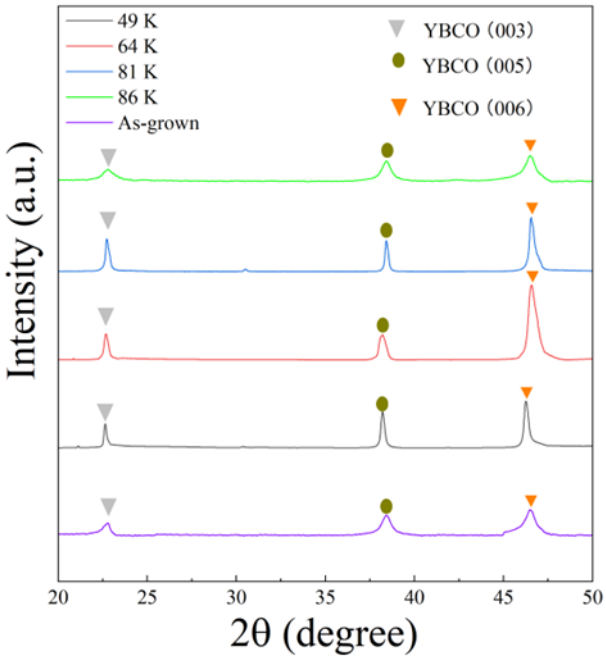

Fig.4.1 XRD patterns of YBCO thin films prepared with different T_c: 49 K, 64 K,81 K, 86 K, and as-grown film.

According to the literature, the c-axis parameter in YBCO expands with increasing oxygen deficiency, particularly in bulk samples where δ ranges from 0 to ~1. To quantitatively evaluate the lattice evolution, we calculated the c-axis lattice constants from the position of the (003) peak using Bragg's law:

$$c=\lambda l/2sin\theta$$

where λ = 1.5406 Å (Cu Kα), and l=3 for the (003) reflection.

The resulting c-axis lengths for samples with T_c = 86 K, 81 K, 64 K, and 49 K are 11.6965 Å, 11.7474 Å, 11.7679 Å, and 11.7781 Å, respectively. This trend is consistent with the findings reported by Liang et al. (2006), who established an empirical correlation between the c-axis lattice parameter and the oxygen deficiency in YBCO single crystals.[48] According to their study, an increase in the c-axis length reflects a reduction in oxygen content, which is associated with a decrease in T_c. In our thin film samples, the calculated c-axis lengths exhibit a monotonic increase as T_c decreases from 86 K to 49 K, indicating a progressive depletion of oxygen. These results align well with the structural trend reported by Liang et al., supporting the validity of our XRD-based analysis.

It should be noted, however, that compared to bulk crystals, the variation in c-axis length in our thin films remains relatively small, even across samples with substantial T_c differences. This observation is consistent with earlier reports by Raven et al., who demonstrated that the c-axis expansion in RF-sputtered YBCO films is typically less than 1%, likely due to substrate-induced strain or epitaxial constraints in the thin-film geometry.[34]

4.1.2 STEM-HAADF Imaging

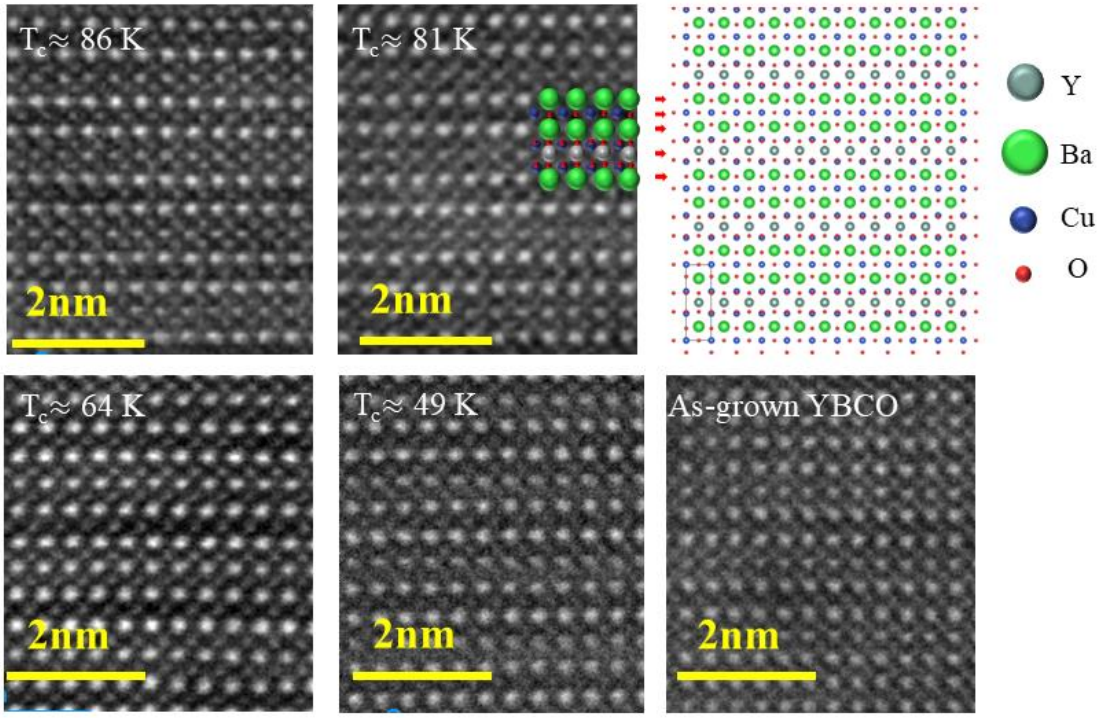

Fig.4.2 High-angle annular dark field (HAADF) images of YBCO, as-grown YBCO $T_c \approx 49$ K, 64 K, 81 K, and 86 K, with the atomic model of the YBCO. In the HAADF images, the brightest spots correspond to barium (Ba, green in the atomic model) atomic columns due to high atomic number (Z-contrast), while the slightly lower spots, to yttrium (Y, gray in the atomic model) atomic columns. Layered in the order of CuO_2 plane, BaO plane, CuO_2 chain, BaO plane, CuO_2 plane, and Y plane along the c-axis corresponding to the vertical direction.

To further examine the local structural features, atomic-resolution HAADF-STEM images were acquired for all samples (Fig.4. 2). The images reveal a well-ordered layered structure consistent with the $YBa_2Cu_3O_7$ unit cell, including identifiable Ba, Y, and Cu atomic columns. The brighter spots correspond to Ba atoms due to Z-contrast, while Y atoms appear slightly dimmer. Each unit cell is composed of CuO_2 planes, Cu–O chains, and intervening BaO and Y layers stacked along the c-axis. These layers are well resolved and consistent across all samples.

Despite substantial changes in superconducting T_c (from 49 K to 86 K), no significant structural distortion or lattice collapse was observed among the samples, including the as-grown oxygen-deficient film. This suggests that the oxygen treatments used in this study, ranging from in situ annealing in 30 Pa O_2 to ex-situ annealing at 1 atm, do not induce detectable changes in the atomic framework.

Importantly, due to the relatively small number of oxygen atoms (7 per unit cell) and their lower atomic number, direct imaging of oxygen vacancies is not feasible by HAADF. Furthermore, given that the maximum δ remains below ~0.3 in most samples, the proportion of oxygen-deficient sites is less than one-seventh, rendering intensity differences in the images too subtle to resolve individual oxygen positions. Therefore, to obtain site-specific information on oxygen deficiency, spectroscopic techniques such as

EELS are required, which are addressed in the next section.

4.2 Electronic structure analysis by EELS: O K-edge and Cu L-edge

To confirm the characteristic EELS patterns of oxygen-deficient sites, we compared two reference samples. The first is the as-grown YBCO (oxygen-untreated), which exhibits the characteristic spectrum of oxygen deficiency at the O-K edge. Another sample is the YBCO sample with the lowest oxygen deficiency among the four YBCO samples, with a T_c of 86 K, allowing us to observe the characteristic spectrum when oxygen deficiency is minimal.

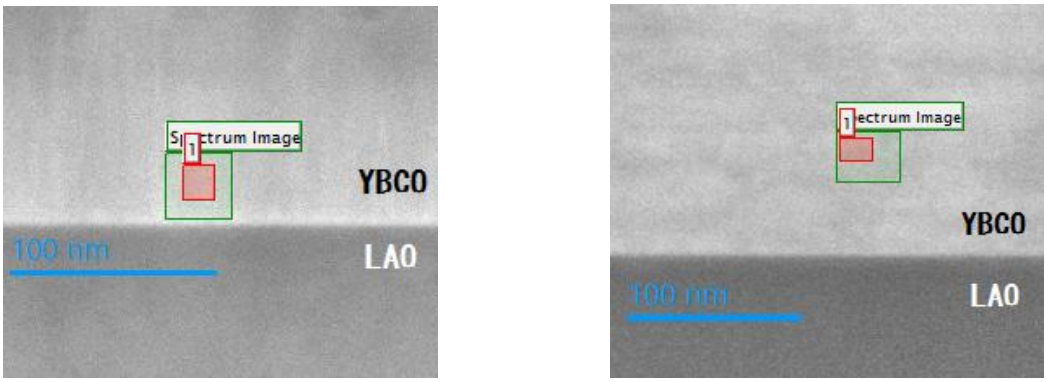

Fig. 4.3 The ADF image near the interface between YBCO and LAO. a, As-grown YBCO. b, YBCO with the $T_c \approx 86$ K. The green rectangle shows the EELS mapping area. The red rectangle shows the part that has been used for the EELS spectrum.

The spectra of the as-grown YBCO and the YBCO with a T_c of 86 K near the O-K edge were obtained from the region indicated by red rectangle in Fig.4.3. The O K-edge spectrum shows a pattern that reflects the local oxygen coordination. The main peak at approximately 532 eV is caused by from transitions from O 1s core states to unoccupied O 2p states hybridized with higher-energy conduction bands,[49] which is observed commonly in various oxide materials and is not sensitive to local oxygen vacancies. On the other hand, the pre-peak around 530 eV reflects the hybrid orbitals of the O 2p state and Cu 3d state and is sensitive to changes in charge distribution due to oxygen deficiency.[44]

Müller et al. observed in $SrTiO_3$ that the O K pre-edge remains sharp at δ (which means the oxygen deficiency in STO) = 0.00 and 0.13 but becomes clearly damped by $\delta = 0.25$. Although they did not explicitly discuss the mechanism, this suggests that even a moderate oxygen vacancy concentration (~8% oxygen loss per unit cell) significantly reduces the pre-peak intensity, likely by disrupting Ti–O orbital hybridization.[50] By projection, a $\delta = 0.25$ in a one-dimensional chain corresponds to a vacancy probability of < 0.1 per chain site – yet this was sufficient to noticeably damped the pre-peak.

In $YBa_2Cu_3O_{7-\delta}$, Nücker et al. used polarization-dependent XAS to demonstrate that the O K-edge pre-peak at the Cu–O chain sites decreases progressively with increasing δ,

with significant damping observed around $\delta \approx 0.4$.[45] While our measurements are based on STEM-EELS, the overall spectral trends are consistent with those observed by XAS, as both techniques probe the unoccupied O 2p–Cu 3d hybridized states responsible for the pre-peak. However, owing to the higher spatial resolution and site-specific sensitivity of STEM-EELS, spectral damping arising from incipient local disruptions in Cu–O hybridization, associated with relatively low levels of oxygen deficiency, can be detected even when bulk-averaged techniques such as XAS show minimal changes.

This interpretation is consistent with the findings of Browning et al., who showed that the pre-peak intensity in the O K-edge spectrum of YBCO decreases with increasing δ. Their data indicate that pre-peak suppression begins to be noticeable from $\delta \approx 0.2$.[46] However, their analysis was based on spatially averaged spectra without resolving chain and plane contributions separately. Moreover, their study did not investigate the relationship between local oxygen deficiency and T_c, which is a key focus of the present work.

As the oxygen deficiency increases, the number of these hybridized states decreases due to the disruption of Cu–O bonding, resulting in a damped pre-peak signal. This provides a physical basis for using pre-peak intensity as an indicator of local oxygen deficiencies. As shown in Fig. 4.4, the YBCO sample with $T_c \approx 86$ K exhibits a well-

developed pre-peak at 530 eV, while the as-grown YBCO shows suppression of the pre-peak, confirming that the reduction in pre-peak intensity reflects increased oxygen deficiency.

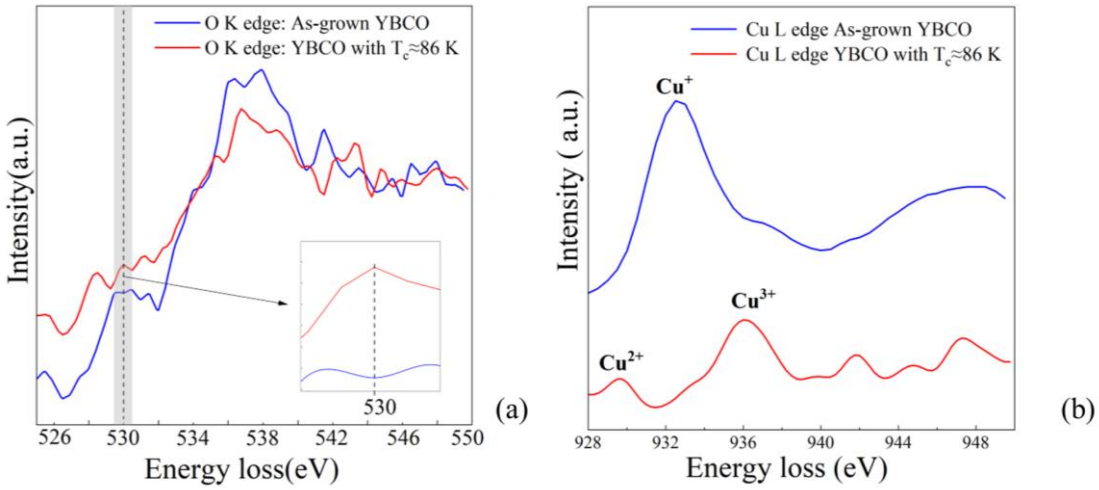

Fig.4.4. EELS of O K edge and Cu L edge of YBCO. (a), EELS of O K edge of YBCO without oxygen treatment and T_c≈86 K. (b), EELS of Cu L_3 edge of YBCO without permeation and T_c≈86 K.

The spectrum pattern at Cu L_3 edge is known to change depending on the Cu valence, thus, the oxidation state of Cu. The valence states of Cu (Cu^+, Cu^{2+}, Cu^{3+}) exhibit different spectral patterns, so it seems easy to identify the valence state of each Cu site. However, even in the YBCO without oxygen deficiency ($YBa_2Cu_3O_7$), the valence states of Cu are

a mixture of +2 and +3 in a 2:1 ratio, making it difficult to identify the valence state of each Cu site. In detail, the Cu in the chain is mainly Cu^{2+}, but the Cu in the CuO_2 plane has a mixed valence state of Cu^{2+}/Cu^{3+}.[51]

In the YBCO with $T_c \approx 86$ K (Fig.4.4(b)), the Cu L-edge spectrum shows two peaks. The 930 eV peak[52] corresponds to Cu^{2+} ($3d^9$) and the 936 eV[53] peak to Cu^{3+} ($3d^8$). On the other hand, in the as-grown YBCO (Fig. 4.4(b)), a clear peak is observed around 931 eV, which corresponds to Cu^{1+} ($3d^{10}$). The peak at 936 eV is relatively low, suggesting a decrease in the Cu^{3+} ratio, thus, a large amount of oxygen deficiencies. The mixing ratio of Cu valence (+1, +2, +3) in the CuO_2 plane and Cu-O chain varies depending on the oxygen deficiency ratio. However, it is impossible to estimate the mixing ratio quantitatively from the Cu L-edge spectrum due to the multiple scattering process of the incident electrons. Therefore, in this study, no local information on oxygen deficiency was obtained from the Cu L-edge spectrum.

4.3. Site-specific oxygen deficiency and T_c

Fig 4.5 shows EELS results of the O K edge at both CuO_2 plane and Cu-O chain sites of the YBCO samples with $T_c \approx 49$ K, 64 K, 81 K, and 86 K, respectively. The O-K edge spectra at the CuO_2 plane and Cu-O chain sites were obtained by scanning the electron

probe along the CuO_2 planes or Cu-O chain as indicated by line red or blue in Fig4.5 c, respectively. In the case of $T_c \approx 86$ K, the pre-peak of 530 eV is observed at both CuO_2 planes and Cu-O chain sites, suggesting that oxygen deficiency is rare. In the case of Tc ≈ 81 K, it is damped at the Cu-O chain site, while it retains at the CuO_2 plane site. Since the Cu-O chains act as charge reservoirs supplying carriers to the CuO_2 planes, the

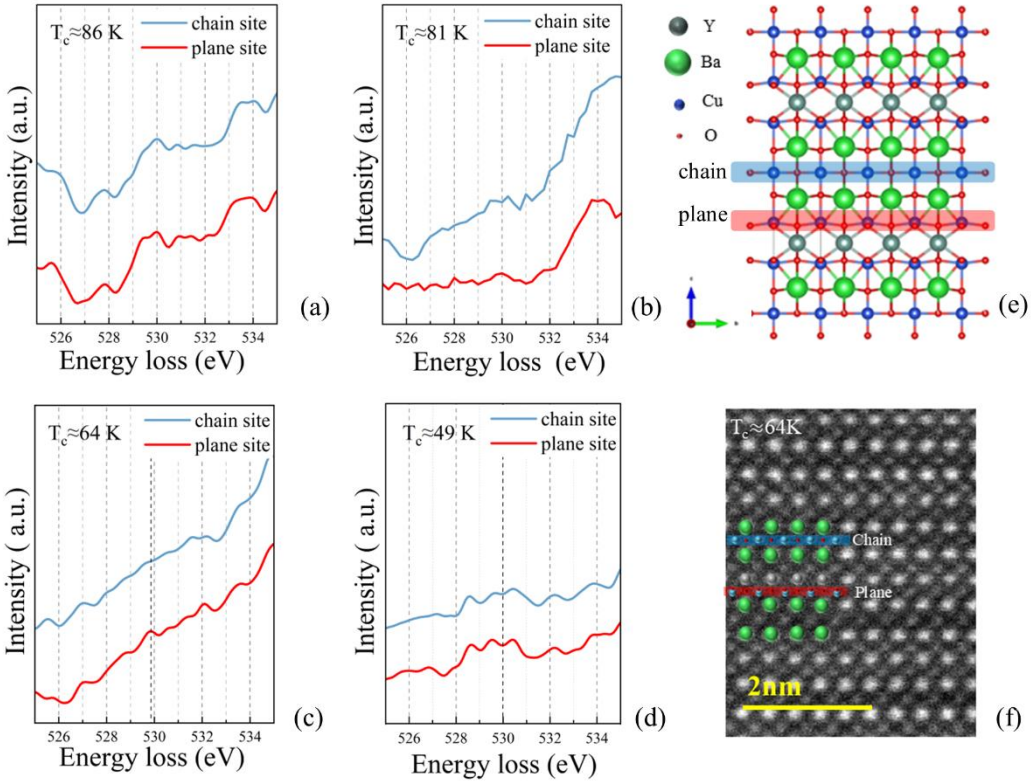

Fig.4.5 (a)-(d) EELS of O K edge at both CuO2 plane and Cu-O chain sites of the YBCO sample with the T_c ≈49 K, 64 K, 81 K, and 86 K, respectively. (e) Structure model of $YBa_2Cu_3O_7$ viewed from the [010] direction. It is constructed by stacking. (f) High-Angle Annular Dark Field (HAADF)-image of YBCO with the T_c ≈64 K

transition temperature, T_c, may decrease due to the oxygen deficiencies at the chain sites. In the case of $T_c \approx 64$ K, the pre-peak of 530 eV is damped at the Cu-O chain site, while it still retains at the Cu-O chain site. Further oxygen deficiencies in the Cu-O chain reduces the role of charge reservoir, resulting in a further decrease in T_c. In the case of Tc ≈ 49 K, the pre-peak of 530 eV is damped at both the Cu-O chain and Cu-O plane sites. Unlike the higher-T_c YBCO samples, the extension of oxygen deficiency into the CuO_2 planes result in a more severe suppression of charge carriers, directly affecting superconducting properties. This result is consistent with the theoretical expectation that the CuO_2 planes are the primary regions responsible for superconductivity,[54,55] and structural or electronic disorder in these planes can influence superconducting behavior.

The YBCO structure consists of Y planes (only yttrium atoms), CuO_2 planes, BaO planes, CuO chains, BaO planes, and CuO_2 planes stacked in order along the c-axis. The CuO_2 planes sandwiched between the Y and BaO planes contain two oxygen atoms, while the CuO chain sandwiched between two BaO planes contains only one oxygen atom in one unit cell. Since there are two CuO_2 planes in the unit cell of $YBa_2Cu_3O_7$, the oxygen atoms at the plane sites account for 4 out of 7 oxygen atoms per unit cell, whereas the Cu–O chain accounts for 1 out of 7. According to neutron diffraction studies by J. D.

Jorgensen et al., the apical oxygen atoms remain nearly fully occupied even when δ approaches 0.5. [43]This suggests that oxygen deficiencies occur primarily at the Cu–O chain and CuO_2 plane sites, and that the apical sites can be excluded from the vacancy distribution analysis.

Based on this structural configuration, and assuming that oxygen atoms are removed randomly from the non-apical sites, a 1:4 distribution of oxygen deficiencies between the chain and the planes is expected. However, this model describes only the statistical probability of where deficiencies might occur, not the actual microscopic distribution. For example, $\delta = 0.2$ corresponds to 0.2 missing O per unit cell on average. In practice, this means most unit cells are intact and ~20% of unit cells have one missing oxygen (rather than every cell having 20% of an oxygen atom missing). If oxygen loss strictly followed the 1:4 ratio, most deficiencies would statistically appear in the CuO_2 planes due to their larger oxygen content. Yet our experimental results diverge significantly from this prediction. By combining the structural model with site-resolved O K-edge EELS spectra, we estimate that the $T_c \approx 81$ K and 64 K samples correspond to approximately 20−30% of the chain oxygen sites vacant (consistent with $\delta \approx 0.2-0.3$), while the 49 K sample reflects an overall $\delta \approx 0.5$, with a portion of the deficiency now extending into the CuO_2 planes.

While the origin of the 60 K plateau in $YBa_2Cu_3O_{7-\delta}$ has been debated in prior studies, our atomic-resolution observations provide direct experimental insight on the site-specific distribution of oxygen deficiencies. Although our measurements do not include a sample with T_c exactly at 60 K, the two samples with $T_c \approx 81$ K and 64 K (corresponding to $\delta \approx 0.2$ and 0.3, respectively) lie just above and at the beginning of the 60 K plateau region, respectively. In both cases, our EELS data reveal that oxygen deficiencies are only in the Cu–O chain sites. It has been reported that only sufficiently long and continuous Cu–O chains can effectively supply holes to the CuO_2 planes.[33,43,56] Therefore, the progressive fragmentation of the Cu–O chains due to oxygen deficiencies may limit hole transfer, and further oxygen loss beyond this point may not significantly alter the hole concentration in the CuO_2 planes, resulting in a plateau in T_c.

4.4 Representativeness of the EELS Analysis Region

One concern raised is whether the EELS analysis region, taken near the film-substrate interface, can be considered representative of the bulk properties, given the potential for local strain or lattice relaxation. Such effects are particularly pertinent in thin film systems, where interfacial mismatch or post-deposition stress may distort the local structure and electronic configuration, thereby compromising comparisons with bulk-sensitive data

such as XRD or transport measurements.

To directly address this concern, we evaluated the structural integrity of the EELS acquisition region using high-angle annular dark-field (HAADF) STEM imaging. As shown in Fig. 4.6 (a), both the EELS analysis area (spectrum 2) and a reference region near the surface (spectrum 1) were acquired from structurally uniform areas, free of visible defects, amorphous zones, or signs of distortion. The atomic columns were clearly resolved, indicating that both locations maintained crystallographic order without significant lattice bending or relaxation.

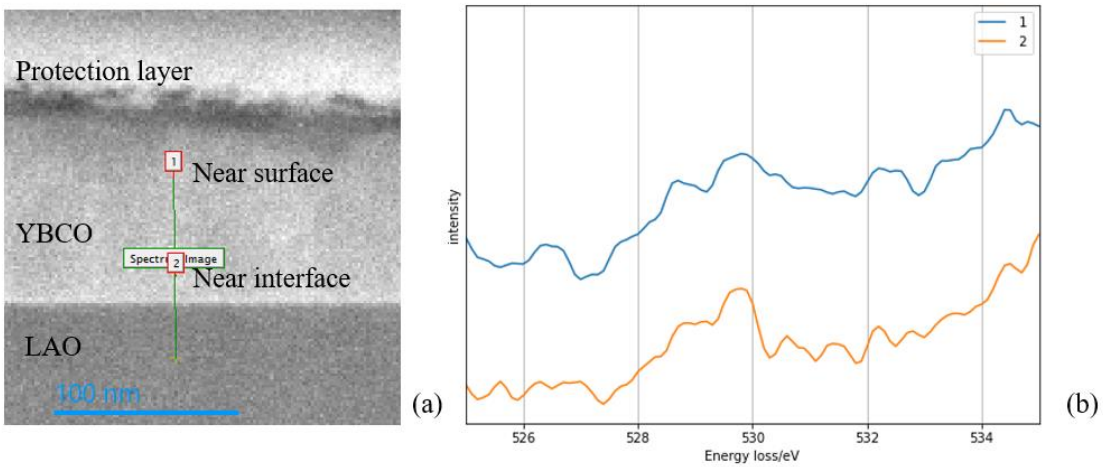

Fig.4.6 EELS line scanning of YBCO. (a) ADF image of YBCO and the scanning line. (b)EELS spectrum of different part in YBCO, 1 represent the part near surface, 2 represent the part near interface.

Moreover, the corresponding O K-edge EELS spectra in Fig. 4.6.(b) display consistent spectral features, including the characteristic pre-peak associated with O 2p–Cu 3d hybridization. Although a minor suppression of the pre-peak is observed in the near-interface region, the overall spectral profile remains qualitatively similar. This subtle variation likely reflects a slight gradient in oxygen content rather than any structural degradation. What's more, as shown in Fig. 4.2, high-resolution HAADF-STEM images acquired from all samples—including the as-grown film and those with T_c of 49 K, 64 K, 81 K, and 86 K, exhibit sharp and periodic atomic columns throughout the imaged area. No significant lattice distortion, dislocation, or interfacial strain contrast was observed in any of the regions where EELS was acquired. This uniform and defect-free atomic structure suggests that the EELS spectra were obtained from structurally relaxed and well-ordered regions, free from the influence of stress-induced distortion typically observed near interfaces.

We therefore conclude that the selected EELS acquisition region is not significantly influenced by strain or relaxation, but instead reflects the intrinsic properties of the film. Furthermore, since the entire lamella was prepared from a representative and defect-free region of the film interior, the observed oxygen deficiency trends are unlikely to arise from interfacial distortion artifacts.

In this context, we consider our thin films to be structurally ideal, and our EELS measurements to effectively probe meaningful oxygen deficiency distributions that can be directly correlated with macroscopic properties such as Tc and XRD-derived lattice constants. The high structural quality evidenced by both HAADF imaging and spectral consistency underscores the representativeness of the analysis area, thus supporting the validity of our conclusions.

4.5 Reproducibility of Site-Specific EELS Spectra at $T_c \approx 49$ K

To address concerns regarding the reliability and reproducibility of the site-specific EELS analysis, particularly the damping observed in the pre-peak of the O K-edge around 530 eV, we conducted an additional set of measurements on a YBCO thin film sample with a superconducting transition temperature of approximately 49 K. Spectra were acquired from two spatially distinct regions of the same sample, both using high-angle annular dark-field (HAADF) STEM imaging to identify CuO chain and CuO_2 plane sites with atomic precision.

Despite differences in dispersion energy settings between the two measurements, 0.1 eV/channel in Fig. 4.7b and 0.25 eV/channel in Fig. 4.7d, the overall spectral shapes remain comparable. While the higher dispersion setting in Fig. 4.7b allows for better

energy resolution and captures finer spectral features, the broader dispersion in Fig. 4.7d still clearly reveals the key difference in pre-peak intensity between the two oxygen sites. This reproducibility across spatially separated regions within the same sample strengthens the credibility of the observed site-specific spectral variation and minimizes the possibility that the trend arises from local noise or experimental artifacts.

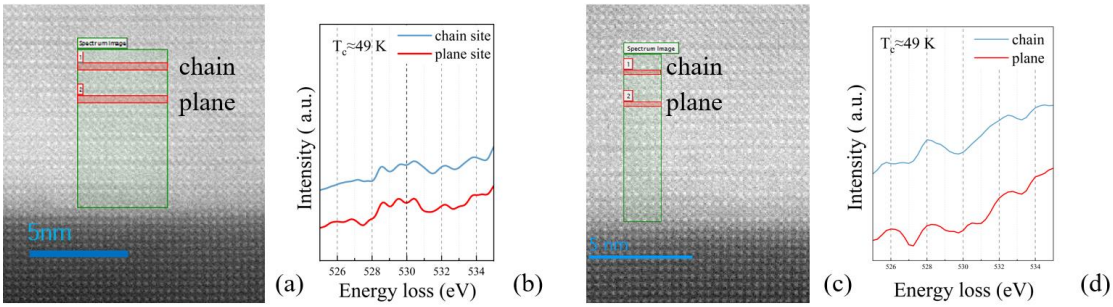

Fig. 4.7 (a) HAADF-STEM image showing the spectrum acquisition area; (b) EELS spectra from chain and plane sites recorded with 0.1 eV/channel dispersion at the region shown in (a); (c) HAADF-STEM image from a different area within the same sample; (d) EELS spectra acquired with 0.25 eV/channel dispersion at the region shown in (c).

It is also important to note that the HAADF images used for site identification show no indication of lattice distortion or relaxation in either region. Therefore, both areas can be

considered structurally representative and unaffected by local strain fields that might otherwise compromise interpretation. These findings reinforce our conclusion that the observed differences in spectral features reflect genuine, site-specific oxygen deficiency effects in YBCO, rather than noise or measurement uncertainty. This reproducibility strengthens the overall argument of this study and enhances the credibility of the EELS-based analysis of local oxygen behavior.

Chapter 5. Conclusion and Outlook

In this dissertation, we conducted a comprehensive investigation into the spatial distribution and site-specific effects of oxygen deficiencies in $YBa_2Cu_3O_{7-\delta}$ (YBCO) thin films, focusing on their correlation with superconducting transition temperature (T_c). Combining advanced characterization techniques, primarily scanning transmission electron microscopy and electron energy-loss spectroscopy (STEM-EELS), with complementary first-principles calculations, we provided both experimental and theoretical insights into how oxygen deficiency evolves at the atomic scale and affects superconducting behavior.

5.1 Summary of Key Findings

- High-resolution STEM-EELS mapping revealed that oxygen deficiencies initially appear in the Cu–O chains and only extend into the CuO_2 planes when δ exceeds approximately 0.4–0.5. This site-selective progression is consistent with the notion that the chains serve as a charge reservoir, while the planes are the primary carrier transport channels in superconductivity.
- The O K-edge pre-peak intensity at ~530 eV was found to be highly sensitive to local oxygen coordination and hybridization. Suppression of this feature served as a

reliable spectroscopic marker of local oxygen deficiency, especially in differentiating between chain and plane site deficiencies.

- By systematically comparing samples with different T_c values (ranging from 49 K to 86 K), we established a clear correlation between the spatial location of deficiencies and superconducting performance. Notably, superconductivity remained relatively robust even with chain deficiencies but declined sharply once the CuO_2 planes became oxygen-deficient.
- To ensure reproducibility and transparency of our spectroscopic analysis, we documented the complete EELS data processing workflow, including zero-loss peak calibration, background subtraction using a power-law model, and raw spectrum inspection prior to smoothing. This methodological appendix enhances the rigor and traceability of our analysis.

5.2 Research Contributions

This work offers a direct visualization of oxygen deficiency distribution at the atomic scale in YBCO thin films and links these structural changes to superconducting properties. The site-specific distinction between Cu–O chain and CuO_2 plane deficiencies provides a refined understanding of the mechanisms behind the well-known nonlinear T_c–δ

relationship and the characteristic 60 K plateau.

Furthermore, by bridging spectroscopic measurements with first-principles calculations, this study exemplifies how experimental data and theoretical modeling can be combined to clarify the energetics and dynamics of point defects in complex oxides.

5.3 Outlook and Future Directions

While the present study offers significant insight, several avenues remain for future exploration:

- Dynamic Evolution of Deficiencies: In situ STEM-EELS under annealing or biasing conditions could reveal how oxygen vacancies migrate or cluster over time, particularly near interfaces.
- Interface and Strain Effects: The role of substrate-induced strain and interfacial electrostatics on oxygen distribution and T_c should be systematically investigated, especially in device-relevant heterostructures.

In conclusion, this study highlights both methodological and scientific novelties. From a methodological perspective, we demonstrate the power of aberration-corrected STEM-EELS as a site-specific, spatially resolved probe capable of detecting subtle electronic structure variations—specifically, pre-peak suppression in the O K-edge—as a signature

of oxygen deficiencies in layered oxides. Unlike conventional ensemble-averaged techniques such as XRD or bulk XAS, the use of atomic-resolution EELS enables the direct identification of deficiency locations within individual Cu–O chains and CuO_2 planes, thereby offering unmatched insight into local defect chemistry.

On the scientific front, our work addresses a long-standing open question in the field of high-temperature superconductivity: how oxygen deficiencies at distinct crystallographic sites influence superconducting behavior. While prior studies have established the importance of oxygen content on Tc, few have resolved the spatial and site-specific dynamics of these deficiencies. By linking local deficiency evolution with superconducting degradation, this study bridges the gap between atomic-scale defect structures and macroscopic electronic properties.

Taken together, these advances not only clarify fundamental mechanisms in high-T_c superconductors but also demonstrate a broadly applicable framework for investigating local non-stoichiometry in other functional oxides.

Reference

1. Onnes, H. K. (1991). Further experiments with Liquid Helium. G. On the Electrical Resistance of Pure Metals, etc. VI. On the Sudden Change in the Rate at which the Resistance of Mercury Disappears. In Through Measurement to Knowledge: The Selected Papers of Heike Kamerlingh Onnes 1853–1926 (pp. 267-272). Dordrecht: Springer Netherlands.
2. Van Delft, D., & Kes, P. (2010). The discovery of superconductivity. Physics today, 63(9), 38-43.
3. Kozhevnikov, V. (2021). Meissner effect: History of development and novel aspects. Journal of Superconductivity and Novel Magnetism, 34(8), 1979-2009.
4. London, F. (1948). On the problem of the molecular theory of superconductivity. Physical Review, *74*(5), 562.
5. Huang, X. Q. (2010). The Physical Origins of the Meissner Effect and London Penetration Depth. arXiv preprint arXiv:1008.4418.
6. Brandt, E. H. (2001). Theory of type-II superconductors with finite London penetration depth. Physical Review B, 64(2), 024505.
7. Prozorov, R., Giannetta, R. W., Carrington, A., & Araujo-Moreira, F. M. (2000).

Meissner-London state in superconductors of rectangular cross section in a perpendicular magnetic field. *Physical Review B*, *62*(1), 115.

8. Bardeen, J., Cooper, L. N., & Schrieffer, J. R. (1957). Theory of superconductivity. Physical review, 108(5), 1175.
9. De Aquino, F. (2012). Superconducting State generated by Cooper Pairs bound by Intensified Gravitational Interaction.
10. Wen, H. H. (2022). Unconventional superconductivity after the BCS paradigm and empirical rules for the exploration of high temperature superconductors. In Journal of Physics: Conference Series (Vol. 2323, No. 1, p. 012001). IOP Publishing.
11. Arulsamy, A. D. (2019). Supercurrent flow with large superconductor gap in cuprates: resurrection of phonon-mediated Cooper pairs. Physica Scripta, 94(5), 055803.
12. Swihart, J. C. (1962). Solutions of the BCS integral equation and deviations from the law of corresponding states. IBM Journal of Research and Development, 6(1), 14-23.
13. Kishore, R., & Lamba, S. (1997). Specific heat jump at the superconducting critical temperature.
14. Choy, T. C., & Stoneham, A. M. (1990). Properties of granular high-Tc superconductors in an effective medium theory. Journal of Physics: Condensed Matter, 2(4), 939.

15. Hamad, R. M., Hamad, M. K., Kunwar, S., & Ziq, K. A. (2024). On the Thermodynamic Properties of FexSe0. 5Te0. 5 Superconducting Single Crystals: An Experimental Study. ECS Journal of Solid State Science and Technology, 13(7), 073012.

16. Wu, S. (2001). MgB_2 Crystallites Much Less Anisotropic than Cuprate HTS. MRS Bulletin, 26(7), 495-495.

17. Mazin, I. I. (2005). Intercalant-driven superconductivity in YbC_6 and CaC_6. Physical review letters, 95(22), 227001.

18. Morris, D. E., Kuroda, R. M., Markelz, A. G., Nickel, J. H., & Wei, J. Y. (1988). Small oxygen isotope shift in $YBa_2Cu_3O_7$. Physical Review B, 37(10), 5936.

19. Zhou, X., Lee, W. S., Imada, M., Trivedi, N., Phillips, P., Kee, H. Y., ... & Eremets, M. (2021). High-temperature superconductivity. Nature Reviews Physics, 3(7), 462-465.

20. Gray, K. E. (2002, January). The phenomenology of high-temperature superconductive materials. In AIP Conference Proceedings (Vol. 608, No. 1, pp. 1154-1162). American Institute of Physics.

21. Waldrop, M. M. (1987). The 1987 Nobel Prize for Physics: in one of the fastest awards on record, the prize goes to the discoverers of high-temperature superconductivity less

than two years after the discovery was made. Science, 238(4826), 481-482.

22. Sato, M., Shamoto, S., Onoda, M., Sera, M., Fukuda, K., Hosoya, S., ... & Imaeda, K. (1987). Single Crystal Studies and Electron Tunneling of $(La_{1-x}M_x)_2\ CuO_{4-\delta}$ (M= Ba and Sr). Novel Superconductivity, 927-934.
23. Hull, J. R. (2003). Applications of high-temperature superconductors in power technology. Reports on Progress in Physics, 66(11), 1865.
24. Bussmann-Holder, A., & Keller, H. (2020). High-temperature superconductors: underlying physics and applications. Zeitschrift für Naturforschung B, 75(1-2), 3-14.
25. Alecu, G. (2004). Crystal structures of some high-temperature superconductors. Romanian Reports in Physics, 56(3), 404-412.
26. Hasan, N., Hafeath, H., & Ahmed, A. (2021). Synthesis and characterization of the bulk YBCO-target of superconducting material. Materials Today: Proceedings, 42, 2268-2272.
27. Kosugi, N., Kondoh, H., Tajima, H., & Kuroda, H. (1989). Cu K-edge XANES of $(La_{1-x}Sr_x)_2CuO_4$, $YBa_2Cu_3O_y$ and related Cu oxides. valence, structure and final-state effects on 1s-4pπ and 1s-4pσ absorption. Chemical physics, 135(1), 149-160.
28. Takigawa, M., Reyes, A. P., Hammel, P. C., Thompson, J. D., Heffner, R. H., Fisk, Z., & Ott, K. C. (1991). Cu and O NMR studies of the magnetic properties of

$YBa_2Cu_3O_{6.63}$ (T_c= 62 K). Physical Review B, 43(1), 247.

29. Maruyama, K., Shinagawa, K., Saito, T., & Tsushima, T. T. T. (1995). Calculation of Absorption Spectra of $YBa_2Cu_3O_{7-\delta}$ by Means of Xα Method. Japanese journal of applied physics, 34(6B), L734.

30. Farneth, W. E., Bordia, R. K., McCarron III, E. M., Crawford, M. K., & Flippen, R. B. (1988). Influence of oxygen stoichiometry on the structure and superconducting transition temperature of $YBa_2Cu_3O_x$. Solid state communications, 66(9), 953-959.

31. Tallon, J. L., Bernhard, C., Shaked, H., Hitterman, R. L., & Jorgensen, J. D. (1995). Generic superconducting phase behavior in high-T_c cuprates: T_c variation with hole concentration in $YBa_2 Cu_3O_{7-\delta}$. Physical Review B, 51(18), 12911.

32. Beyers, R., Ahn, B. T., Gorman, G., Lee, V. Y., Parkin, S. S. P., Ramirez, M. L., ... & Huggins, R. A. (1989). Oxygen ordering, phase separation and the 60-K and 90-K plateaus in $YBa_2Cu_3O_x$. Nature, 340(6235), 619-621.

33. Cava, R. J., Batlogg, B., Chen, C. H., Rietman, E. A., Zahurak, S. M., & Werder, D. (1987). Oxygen stoichiometry, superconductivity and normal-state properties of $YBa_2Cu_3O_{7-\delta}$. Nature, 329(6138), 423-425.

34. Raven, M. S., Inametti, E. E., Wan, Y. M., & Murray, B. G. (1994). c-axis expansion in RF sputtered $YBa_2Cu_3O_x$ thin films. Superconductor Science and Technology, 7(7),

462.

35. Liang, R., Bonn, D. A., & Hardy, W. N. (2006). Evaluation of CuO_2 plane hole doping in $YBa_2 Cu_3O_{6+x}$ single crystals. Physical Review B—Condensed Matter and Materials Physics, 73(18), 180505.

36. Zaleski, T. A., & Kopeć, T. K. (2006). Possible origin of 60-K plateau in the $YBa_2Cu_3O_{6+y}$ phase diagram. Physical Review B—Condensed Matter and Materials Physics, 74(1), 014504.

37. He, A. Q., Zhou, G. F., Qiao, G. W., & Ye, H. Q. (1992). Microstructure and superconductivity of YBCO by the melt-spun-texture-growth method. Materials Letters, 13(6), 373-376.

38. Suematsu, H., Okamura, H., Nagaya, S., & Yamauchi, H. (1998). "Large-Area TEM" Observation of the Distribution of Y-211 Particles in YBCO Superconductors Melt-Grown under Varying Oxygen Pressure. In Advances in Superconductivity X: Proceedings of the 10th International Symposium on Superconductivity (ISS'97), October 27–30, 1997, Gifu Volume 1–3 (pp. 661-664). Springer Japan.

39. Basu, S. N., Roy, T., Mitchell, T. E., & Nastasi, M. (1989). Electron Beam Induced Oxygen Disordering in Yba2cu307-X Superconductors. MRS Online Proceedings Library (OPL), 157, 581.

40. Degoy, S., Jimenez, J., Martin, P., Martinez, O., Prieto, A. C., Chambonnet, D., ... & Perriere, J. (1996). Oxygen content of YBaCuO thin films. Physica C: Superconductivity, 256(3-4), 291-297.

41. Benzi, P., Bottizzo, E., & Rizzi, N. (2004). Oxygen determination from cell dimensions in YBCO superconductors. Journal of crystal growth, 269(2-4), 625-629.

42. Yurtcan, M. T., Simsek, O., Yilmaz, M., Hasar, U. C., Ertugrul, M., & Bayram, O. S. (2013). Influence of Deposition Pressure (O_2) on the YBCO (Y123) Thin Films Prepared by Pulsed Laser Deposition. Journal of superconductivity and novel magnetism, 26, 1873-1877.

43. Jorgensen, J. D., Veal, B. W., Paulikas, A. P., Nowicki, L. J., Crabtree, G. W., Claus, H., & Kwok, W. K. (1990). Structural properties of oxygen-deficient $YBa_2Cu_3O_{7-\delta}$. Physical Review B, 41(4), 1863.

44. Van Aken, P. A., Liebscher, B., & Styrsa, V. J. (1998). Core level electron energy-loss spectra of minerals: pre-edge fine structures at the oxygen K-edge: Comment on “Water in minerals detectable by electron energy-loss spectroscopy EELS” by R. Wirth, Phys Chem Minerals (1997) 24: 561–568. Physics and Chemistry of Minerals, 25, 494-498.

45. Nücker, N., Pellegrin, E., Schweiss, P., Fink, J., Molodtsov, S. L., Simmons, C. T., ...

& Müller-Vogt, G. (1995). Site-specific and doping-dependent electronic structure of $YBa_2Cu_3O_x$ probed by O 1s and Cu 2p x-ray-absorption spectroscopy. Physical Review B, 51(13), 8529.

46. Browning, N. D., Yuan, J., & Brown, L. M. (1992). Determination of the local oxygen stoichiometry in $YBa_2Cu_3O_{7-\delta}$ by electron energy loss spectroscopy in the scanning transmission electron microscope. Physica C: Superconductivity, 202(1-2), 12-18.
47. Pennycook, S. J., & Nellist, P. D. (Eds.). (2011). Scanning transmission electron microscopy: imaging and analysis. Springer Science & Business Media.
48. Liang, R., Bonn, D. A., & Hardy, W. N. (2006). Evaluation of CuO_2 plane hole doping in $YBa_2Cu_3O_{6+x}$ single crystals. Physical Review B—Condensed Matter and Materials Physics, 73(18), 180505.
49. Colliex, C. (2022). From early to present and future achievements of EELS in the TEM. The European Physical Journal Applied Physics, 97, 38.
50. Muller, D. A., Nakagawa, N., Ohtomo, A., Grazul, J. L., & Hwang, H. Y. (2004). Atomic-scale imaging of nanoengineered oxygen vacancy profiles in $SrTiO_3$. Nature, 430(7000), 657-661.
51. Temmerman, W. M., Winter, H., Szotek, Z., & Svane, A. (2001). Cu valency change induced by O doping in YBCO. Physical Review Letters, 86(11), 2435.

52. Chen, H., Callaway, J., & Misra, P. K. (1988). Electronic structure of Cu-O chains in the high-T_c superconductor Y $Ba_2Cu_3O_7$. Physical Review B, 38(1), 195.

53. Gleason, S. P., Lu, D., & Ciston, J. (2024). Prediction of the Cu oxidation state from EELS and XAS spectra using supervised machine learning. npj Computational Materials, 10(1), 221.

54. Shen, Z. X., Allen, J. W., Yeh, J. J., Kang, J. S., Ellis, W., Spicer, W., ... & Geballe, T. H. (1987). Anderson Hamiltonian description of the experimental electronic structure and magnetic interactions of copper oxide superconductors. Physical Review B, 36(16), 8414.

55. Orenstein, J., & Millis, A. J. (2000). Advances in the physics of high-temperature superconductivity. Science, 288(5465), 468-474.

56. Salluzzo, M., Ghiringhelli, G., Cezar, J. C., Brookes, N. B., De Luca, G. M., Fracassi, F., & Vaglio, R. (2008). Indirect electric field doping of the CuO_2 planes of the cuprate $NdBa_2Cu_3O_7$ superconductor. Physical Review Letters, 100(5), 056810.

Acknowledgement

First and foremost, I would like to express my deepest gratitude to my academic supervisor, Prof. Yoshifumi Oshima, for his invaluable guidance, continuous support, and insightful discussions throughout the course of my doctoral studies. His rigorous approach to research and unwavering encouragement have been instrumental to the completion of this dissertation.

I am also deeply grateful to Assoc. Prof. Jiqiang Jia for generously providing the YBCO thin film samples and for his collaborative support, which laid the foundation for the experimental part of this work.

Special thanks go to Dr. Tongmin Chen, who patiently taught me how to operate the STEM equipment and provided crucial technical assistance during the data acquisition and analysis phases.

Finally, I would like to extend my sincere appreciation to the members of my dissertation committee: Prof. Mikio Koyano, Assoc. Prof. Kenta Hongo, Assoc. Prof. Masashi Akabori and Assoc. Prof. Itsuhiro Kakeya, for their valuable comments, constructive suggestions, and support during the evaluation of this work.

Achievements

Conference

- **Xiaopeng Liu**[1], Yoshifumi Oshima[1], Jiqiang Jia[2] *An EELS study on the relationship between oxygen deficiency sites and transition temperature of YBCO.* 72th JSAP spring meeting 2025. (oral)
- 2.**Xiaopeng Liu**[1],Oshima[1] *A study on Zr addition to $LiCoO_2$ cathode to improve battery performance* 84th JSAP autumn meeting 2023 (poster)

Paper

- Jiqiang Jia[1], Jingran Li [1], **Xiaopeng Liu** [2], Yoshifumi Oshima [2], LiLei [2] *Study of the resistive switching properties of $YBa_2Cu_3O_{7-x}$/Nb:$SrTiO_3$ heterostructures.* Materials Science and Engineering: B Volume 314, April 2025, 118001

Scholarship

澁谷学術文化スポーツ振興財団奨学金